Natural Hazards
https://doi.org/10.1007/s11069-025-07705-2

ORIGINAL PAPER

Hybrid pixel-based and object-based image analysis approach for landslides rapid mapping: the extreme rainfall in Emilia-Romagna (Italy) May 2023 case study

Federico Filipponi[1] · Carla Iadanza[2] · Valerio Vivaldi[3] · Francesco Zucca[3] · Claudia Meisina[3] · Maria Francesca Ferrario[4] · Alessandro Trigila[2]

Received: 22 November 2024 / Accepted: 15 September 2025

Abstract

Landslide rapid mapping inventory, generated in the immediate aftermath of severe landslide events, represents essential information for quantitative landslide risk assessment. It can support effective and efficient response in case of emergency activations, for example by identifying the potential number of affected infrastructures (e.g. roads, railways), and can provide useful information to prioritize the interventions and to guide field survey operations. Additionally, it may represent the base to be used for generating and updating landslide mapping inventories. This research presents a hybrid pixel-based and object-based image analysis approach for landslides rapid mapping using remote sensing optical multispectral imagery. The fully automated supervised procedure relies on change detection analysis, based on quantitative variation of vegetation cover, and can be applied to both aerial imagery and multiple satellites constellations acquisitions at high and very-high spatial resolution. The main novelties rely on the use of an advanced spatial filtering approach, to optimize the removal of commission errors, and a confidence measure, computed using object-oriented image analysis as a solution to optimize the accuracy of the mapping product. Investigated case study for development and testing of the procedure is the heavy rainfall event that hit Emilia-Romagna region (Italy) during May 2023. Satellite imagery acquired by Sentinel-2 and PlanetScope satellites constellations were used to generate rapid mapping products. Validation against two landslides event inventories mapped manually shows increased accuracy of the generated rapid mapping product by applying various threshold values to the confidence measure.

Keywords Rapid mapping · Landslides detection · Remote sensing · Rainfall-induced landslides · Object-based image analysis

Extended author information available on the last page of the article

Published online: 03 October 2025

1 Introduction

Inventories of landslide events are commonly carried out using several input materials, like geomorphological mapping, topographic maps, and aerial photography (Parise 2001), spaceborne and airborne remote sensing imagery (Guzzetti et al. 2012), including interferometric SAR (Schlögl et al. 2022). A comprehensive overview of techniques to map landslides is described by Novellino et al. (2024), that proposed a discrimination in the following categories: change detection; indexing; segmentation; displacements-measurement; and artificial intelligence.

The change detection approach, which is the main used technique, consists of manual mapping by expert operator, which identifies presence of landslide features resulting from a slope failure and reflected in the geomorphology, using remote sensing imagery interpretation, usually of a pair of pre- and post-event acquisitions. The indexing technique is a pixel-based method relying on the use of thresholding of parameters, like the Normalised Difference Vegetation Index (NDVI) (Fiorucci et al. 2019; Notti et al. 2023; Satriano et al. 2023), topographic parameters (Scheip and Wegmann 2021), or SAR back-scatter values and coherence (Burrows et al. 2020). Segmentation technique is an object-based image analysis (OBIA) approach consisting in grouping a number of pixels into shapes with a meaningful representation of the objects based on homogeneous spectral, textural, morphological, and topographical characteristics (Amatya et al. 2021). Since the segmentation ruleset is created based on site-specific characteristics, it might not work in other geographic areas. Displacement-measurements include Interferometric Synthetic Aperture Radar (InSAR) and are not always applicable due to the maximum detectable displacements and topographic constraints (van Natijne et al. 2022).

Artificial intelligence is a promising approach, that allows to map landslides by training data-driven models on a variety of parameters. Convolutional Neural Networks trained on a combination of inventories was found to have a better generalization performance, with a bias towards high precision and low recall scores (Prakash et al. 2021). However, limitation in the use of artificial intelligence methods is the need of large training dataset and computational power.

Examples of semi-automatic identification of areas affected by landslides, by comparing pre- and post-event satellite optical images, are increasingly common in the literature (Mondini et al. 2011; Uehara et al. 2022; Notti et al. 2023; Satriano et al. 2023). Considering that a transition from vegetated to bare soil is usually expected after a landslide, the NDVI changes in time are indeed a powerful indicator, with negative values indicating a decrease in vegetation. Although semi-automatic methods based on change detection analysis are rapid and cost-effective, several limitations do exist, resulting in a limited overall accuracy of the landslides mapping product. For example, critical aspects related to the use of the NDVI are: (i) the optimal definition of thresholds (low threshold values can generate a proliferation of false positives, while high values can produce a reduction in the detection accuracy (Satriano et al. 2023)); (ii) the natural variability over time of the NDVI signal in unperturbed conditions (non-landslide event); (iii) the difficulty of removing false positives, especially when they correspond to riverbank erosions or cultivated land (Notti et al. 2023). In addition to pixel-based approaches, the OBIA approach, based on the concepts of image segmentation and classification using a combination of spectral, shape and contextual information, has been used for semi-automatic mapping of landslides in mostly small-sized study areas or even tailored to single landslides (Martha et al. 2010; Lu et al. 2011; Hölbling et al. 2017). Supervised workflow combining OBIA and machine learning algorithms has been also proposed (Stumpf and Kerle 2011).

Rapid mapping in the immediate aftermath of severe landslide events is crucial to identify the most severely affected areas to prioritize damage assessments and guide field survey operations (Notti et al. 2024).

The present work presents a fully automated supervised procedure for rapid mapping of landslides, in the form of Potential Landslides (PL), suitable to be used in the immediate aftermath of the triggering event. PL represent spatial distribution of areas potentially affected by landslides movements, including source, transit and depositional areas, mapped from remote sensing acquisitions using a supervised procedure, that allows to identify and later refine areas characterized by a decrease in vegetation cover. Considering that the decrease in vegetation cover may be the result of causes other than landslides, such as agricultural practices or other disturbance agents, the identified areas may partly represent territories where no landslide occurred, and here comes the adjective potential. The procedure combines pixel-based and OBIA approaches, and it was designed to be used operationally with both aerial imagery and multiple satellites constellations acquisitions at high and very-high spatial resolution. In addition to the hybrid approach, the main novelties include the use of advanced spatial filtering approach, to optimize the removal of commission errors, and a confidence measure, computed using object-oriented image analysis as a solution to optimize the accuracy of the mapping product.

The investigated case study for development and testing of the procedure is the heavy rainfall event that hit Emilia-Romagna (ER) region (Italy) during May 2023. We compared the obtained PL rapid mapping product with two landslides event inventories mapped manually, and explored the influence of slope and land cover, observing that most of the slope movements are newly formed instabilities rather than reactivations.

The approach here proposed could be applied elsewhere; in particular, the user could fine-tune the model parametrization (input data, selected confidence thresholds) to make it more appropriate to the local setting.

2 Study area

2.1 Geological and geomorphological setting

The study area (Fig. 1) covers almost 9000 km^2, involving the mountainous/hilly region of northern Italian Apennines, of which the largest portion is in ER region (provinces of Bologna, Forlì-Cesena, Modena, Rimini, Reggio nell'Emilia, Ravenna), including small portions of Marche (Pesaro and Urbino province) and Tuscany (Florence and Arezzo provinces) regions. The mountainous/hilly region extends from the SW sector of the Apennine ridge, where Mt. Cimone represents the highest top (2,165 m a.s.l), to NE sector, where the Pede-Apennine margin height ranges from 100 to 200 m a.s.l. Northern Apennines are a fold and thrust belt, developed during the Early to Middle Miocene collisional phase, from the subduction accretionary prism rise (Segoni et al. 2020). The Tuscan Domain and Umbro-Marchigiano-Romagnola Succession units, as well as the so-called allochthonous units, combine to form the Northern Italian Apennine (Castronuovo 2005). The Variscan base-

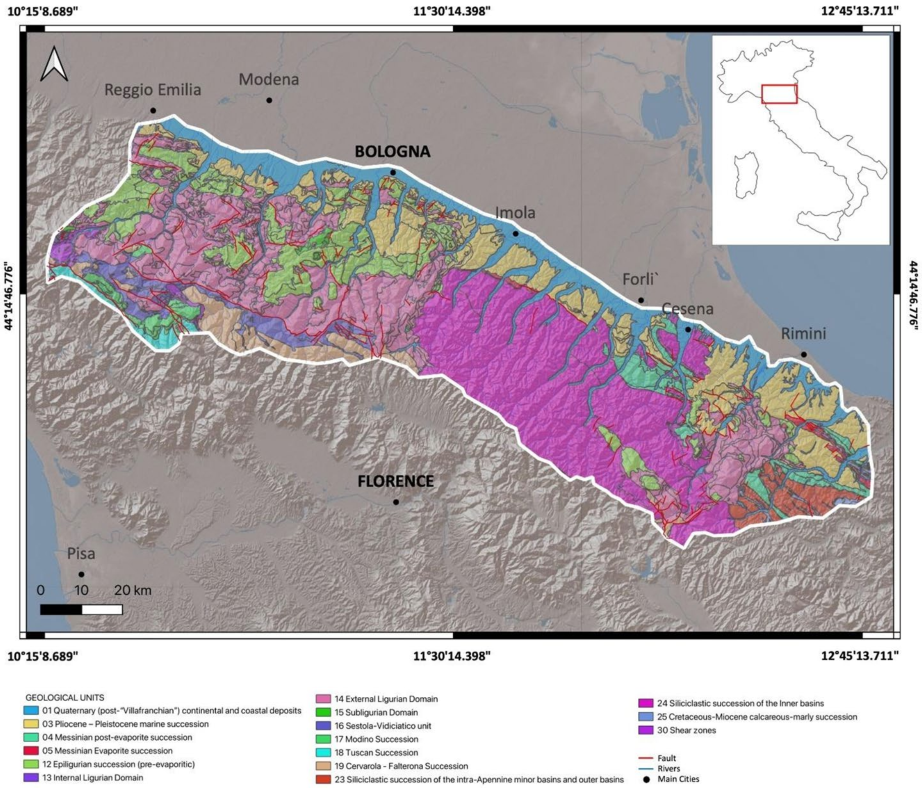

Fig. 1 Geological, geomorphological and structural map of northern Apennines, comprehending the study area (AOI) (CARG—Cartografia Geologica—ISPRA)

ment and its Permian to Cenozoic cover were involved in the deformation of the continental border of the Adria (Apulia) plate, which gave rise to the Tuscan-Umbria units (Carmignani et al. 2004, and references therein). These successions, which are made up of marine and continental deposits in the Emilian Apennine margins, show a regressive nature when compared to the Po River plain. Deposits dated from the higher Miocene to the Pleistocene periods represent the filling of the Apennine deformed graben (Pieri and Groppi 1981), while the most recent deposits are related to the interplay of sedimentation and tectonic forces; the latter are nowadays represented by a compressive tectonic regime.

The main three allochthonous units are Ligurian, Sub-Ligurian and Tuscan-Umbria-Romagna. The Ligurian-Piedmont Ocean (Alpine Tethys) deformation, during the Cretaceous and Paleogene tectonic phases, is the source of the Ligurian units. The Ligurian units, also known as the "Argille Scagliose" (Late Jurassic to the Early Eocene), are made up of tectonic and sedimentary units and are composed of mostly arenites and limestones embedded in a shale/clay matrix (Medley and Goodman 1994). Due to strong tectonic stresses, "Argille Scagliose" formations lost their original well-layered structure that, combined with the high clay content and the block-in-matrix rocks structure, make these chaotic formations the primary cause of landslides. The high shale and clay content of Helmintoid Flysch makes it extremely vulnerable to weathering processes, resulting in thick colluvial deposits where erosion and landslides are frequently encountered (Montrasio et al. 2011). The area of interest (AOI) considered for the analysis (Fig. 1) was delimited based on: (i) mountain-hill orographic model, developed by ISPRA using the digital terrain model TINItaly 10 m (Tarquini et al. 2023; accessed at https://tinitaly.pi.ingv.it/Download_Area1_1.html); (ii) watershed boundaries; (iii) map of cumulative rainfall in the period May 1–17, 2023.

2.2 Rainfall events description

From the May 1, 2023, to May 17, 2023, two rainfall events occurred (Antolini et al. 2016; Arpae-SIMC 2023a; Arpae-SIMC 2023b; Arpae-SIMC 2023c; Arpae-SIMC 2023d). The first event, between May 1st and 3rd, was characterized by persistent rainfalls which produced cumulative rainfall greater than 200 mm for three days (Arpae-SIMC 2023a). Despite the high cumulative precipitation values, the precipitation rate intensity varied from weak to moderate (from 2–4 mm/h up to 15–20 mm/h), due to the stratiform typology of the meteorological phenomena, recording low cumulative values per hour: it was the duration of the event (more than 48 continuous hours) that determined such high cumulative precipitation values. Comparing the cumulative rainfall data over the entire regional territory, it was the most intense recorded for 48 consecutive hours since 1997, and the most intense in the spring season since 1961 (beginning of the homogeneous series of precipitation data on the regional territory). The 48 h cumulative rainfalls are the maximum of the historical series for 27 stations out of 45, even on stations with data series close to 100 years. On May 1, 2023, the rain gauges of the ER regional network recorded 4 h cumulative values lower than 70 mm, with a maximum value of 66.8 mm/24 h in Guiglia (MO). On May 2, 2023, many stations measured cumulative daily rainfall values greater than 80–100 mm, mainly in the central-eastern sector of the region, leading the 24-h cumulative rainfalls above 80 mm and, in some cases, above 180-200 mm. On May 3, 2023, the phenomena maintained weak-moderate intensity and ran out over the course of the week (Arpae-SIMC 2023a).

A second event occurred between May 16, 2023, and May 17, 2023, with cumulative rainfall exceeding 250 mm. As in the first event, rainfall was concentrated in the central-eastern hilly and foothill areas, with maximum cumulative precipitations of 260.8 mm/48 h in Monte Albano, 254.8 mm/48 h in Trebbio and 254.6 mm/48 h in San Cassiano sul Lamone stations. After the two events the total cumulative precipitation for 17 days was over 300–400 mm, with peaks of 609.8 mm in Trebbio (Modigliana municipality, Lamone basin), and 563.4 mm in Le Taverne (Fontanelice municipality, Santerno basin), becoming the record for over 65% of the rain gauges in the area.

Extreme floods occurred during the rainfall events, provoking huge and extensive effects on all the hilly drainage network, mainly on the central-eastern sector of the region, with intense erosion and solid transport phenomena, damage to hydraulic works as well as localized flooding and broken banks (Arpae-SIMC 2023b; Arpae-SIMC 2023d).

Several landslides occurred in the study area, mainly in the provinces of Bologna, Ravenna and Forlì-Cesena; they temporarily affected infrastructures, damaged buildings, and even caused one victim. From the first event, widespread small shallow landslides occurred, accompanied by runoff and debris transport (Arpae-SIMC 2023c).

During the two events time span some wide landslides occurred, nearby the areas interested by the highest values of cumulative rainfall. The distribution of the phenomena reflects indeed the trend of rainfall accumulations: the phenomena occurred most frequently in the hilly and low mountain areas.

3 Landslides inventories

3.1 Pre-event landslides inventory (IFFI)

The pre-event (May 2023) landslides, recorded in the Italian Landslide Inventory—IFFI over the AOI, are 58,825 and affect an area of 1,872 km^2; the most frequent types of movement are slides (42.5%), slow earth flows (28.7%) and complex landslides (18.2%). Landslides have an average area of about 32,000 m^2 and a maximum value of 4.9 million m^2. If we consider the entire territory of the ER region, pre-event landslides amount to 80,335 and affect a total area of 2,768 km^2. The landslide index (ratio between landslide area and regional area) is equal to 12.3%; if we consider exclusively the mountainous-hilly territory the ratio reaches 24.6%.

The Italian Landslide Inventory—IFFI, carried out by ISPRA and the Regions and Autonomous Provinces, contains landslides that occurred on the national territory, recorded according to a standardized and shared methodology. Data can be viewed and downloaded from the IdroGEO web platform (https://idrogeo.isprambiente.it/app/iffi, Iadanza et al. 2021, see supplementary material Fig. S1). The methodology is based on historical and archival data, on aerial and satellite imagery interpretation, on land surveys, on a Landslide Data Sheet for collecting information, and on 1: 10,000 mapping scale. Each landslide is represented by a point (Landslide Identification Point) located at the landslide crown, by a polygon or by a line, when the width of the landslide cannot be mapped (e.g. rapid debris flows) (Trigila et al. 2010).

In the AOI, slides occur mainly in lithologies dominated by alternations between rocks (sandstones and calcarenites mainly) and marly pelites or pelites. Slow earth flows are found on predominantly clayey lithologies in the medium-lower part of the Emilian Apennines and in the lower Romagna hills. The complex type represented by deep landslides, constituted by rotational slides evolving in slow earth flow, is particularly frequent in the middle Apennines set on fractured arenitico-pelitic alternations in correspondence with the Ligurian Flysch (Gozza and Pizziolo 2007).

Most of the landslides, particularly those of large dimensions (> 1 ha), show persistence over time, with periods of quiescence lasting many years or centuries alternating with mass remobilizations during rainfall events.

3.2 Ferrario event inventory

The landslide inventory of the May 2023 event, which was used as reference event inventory, was realized through manual mapping, by expert operator visual inspection of PlanetScope satellite imagery. Pre-and post-event images were visualized directly in QGIS software, taking advantage of the Planet QGIS plugin. The April 2023 basemap provided by Planet was used as pre-event imagery, while cloud-free images (PlanetScope level 3B) acquired between May 22, 2023, and mid-June 2023 were used as post-event images. The inventory thus covers both the May 1–3, 2023, and May 16–17, 2023, rainfall events.

The inventory covering a 5,764 km^2 area was made available online on June 30, 2023 (https://zenodo.org/records/8102429) and presented by Ferrario (2023); here we enlarged the mapped area, to analyze the same AOI investigated with automatic mapping methods, reaching a dimension of about 8,981 km^2. Additionally, we double-checked the polygons located in flat regions (slope < 5°, which account for about 2% of the polygons of the first inventory), removing false positives, generally associated with river erosion and not due to gravity movements. Landslide mapping was realized by a single expert operator at a scale of 1:5,000; no distinction between source or deposit areas, nor a classification of the slope movements was attempted.

The inventory realized manually includes 49,103 landslides over an 8,981 km^2 area, resulting in an average density of 5.5 landslides/km^2. The landslide area amounts to 40 km^2, covering 0.44% of the whole AOI. Landslides have an average area of 815 m^2 and a maximum value of about 100,000 m^2. The dataset is publicly available at https://zenodo.org/records/13234762 (Ferrario 2024).

The improvement with respect to the inventory by Ferrario (2023) lies in the mapping of a wider area, covering the entire AOI, where almost 3,000 additional landslides were mapped. Despite the large increase in the mapped area, the number of landslides is not significantly higher, thus suggesting that the first inventory already surveyed the area most affected by landslide phenomena. The analysis of predisposing factors (Ferrario and Livio 2024) showed a higher frequency of landslides on steeper slopes and on outcropping rocks or badlands; a slightly positive correlation was obtained for the silty and flysch-like lithological units.

3.3 ER region event inventory

Additional reference event inventory is the landslide inventory of the May 2023 event realized by the Emilia-Romagna Region—Geological Survey, the University of Bologna and the University of Modena and Reggio Emilia (Berti et al. 2025). Such inventory covers only the ER region territory, was carried out through photointerpretation of high-resolution aerial (RGBI orthophotos at 20 cm/px—May 2023 by CGR S.p.A.) and satellite imagery, locally integrated with field surveys. The inventory contains 80,194 landslides with a landslide area of 83.33 km^2. Landslides have an average area of 1,039 m^2 and a maximum value of about 500,000 m^2.

Landslides, represented with polygonal geometries, are classified into: rapid earth and/or debris slides; non-channeled earth and/or debris flows; channeled earth and/or debris flows; mudflows; translational and/or rotational slides; translational rock slides on a bedding plane; complex landslides; rockfalls or rockfalls/slides (Brath et al. 2023). The ER region event inventory, first published on March 18, 2024 and last updated in June, 2024, is freely available online at: https://datacatalog.regione.emilia-romagna.it/catalogCTA/dataset/r_emiro_2024-03-26t095445.

4 Methodology

PL detection approach relies on the indexing methods and change detection analysis, based on quantitative variation of vegetation spectral index calculated from pairs of remote sensing images acquired before and after the event. Areas characterized by a decrease in vegetation cover are further processed, using a combined pixel-based and OBIA approach, to produce PL rapid mapping product.

The detection procedure involves a data analysis (Fig. 2) consisting of the following main steps: (i) pre-processing, to prepare and harmonize datasets; (ii) processing, for the detection of PL; (iii) post-processing steps, for the generation of mapping product and statistics.

4.1 Pre-processing

Considering that the proposed methodological approach aims to map landslides as early as possible from optical multispectral imagery, a single post-event satellite acquisition, the first one available with a sufficient number of cloud-free pixels, is used for the analysis. Diversely, a mosaic of multiple satellite acquisitions acquired on different days can be used as a pre-event reference imagery, in order to reduce the number of missing pixels due to cloud cover. In order to minimize the number of false positives, related to changes in vegetation cover that are not caused by landslides, it is necessary to secure a time interval as short as possible between pre-event and post-event acquisitions.

Input data used for the analysis are bottom of atmosphere reflectance acquired by optical multispectral satellite sensors. Spectral bands corresponding to the radiometric range of green, red, and near-infrared are needed for subsequent data analysis steps, that consists in the calculation of spectral indices. Optionally, ancillary masks provided with each satellite dataset, corresponding for example to cloud cover, cloud shadows, and pixels outside the sensor acquisition footprint, can be used to generate the pixel masks, that are applied to mask out bad pixels from further analysis. In case more than one scene is available for an acquisition date, mosaics of single masked spectral bands and pixel masks are then generated for each date of acquisition and each sensor. The mosaics acquired on different days before the event can be later used to generate a single pre-event composite image, to reduce missing pixels due to cloud cover. Another optional pre-processing step is the image co-registration, that can be used to improve spatial coherence. Among the available algorithms, AROSICS (Scheffler et al. 2017) has been demonstrated to well perform, thanks to the availability of local co-registration approach. When using co-registration to improve imagery spatial consistency, post-event image scene, mosaic or composite should be used as master. Final data pre-processing step is the calculation of Normalized Difference Vegetation Index (NDVI) (Rouse et al. 1974) (Eq. 1) and Normalized Difference Water Index (NDWI) (McFeeters 1996) (Eq. 2) from masked spectral bands, to obtain final datasets consisting in a single pre-event masked NDVI raster and single NDVI and NDWI post-event raster, covering the entire AOI.

$$NDVI = \frac{(near\ infrared - red)}{(near\ infrared + red)} \tag{1}$$

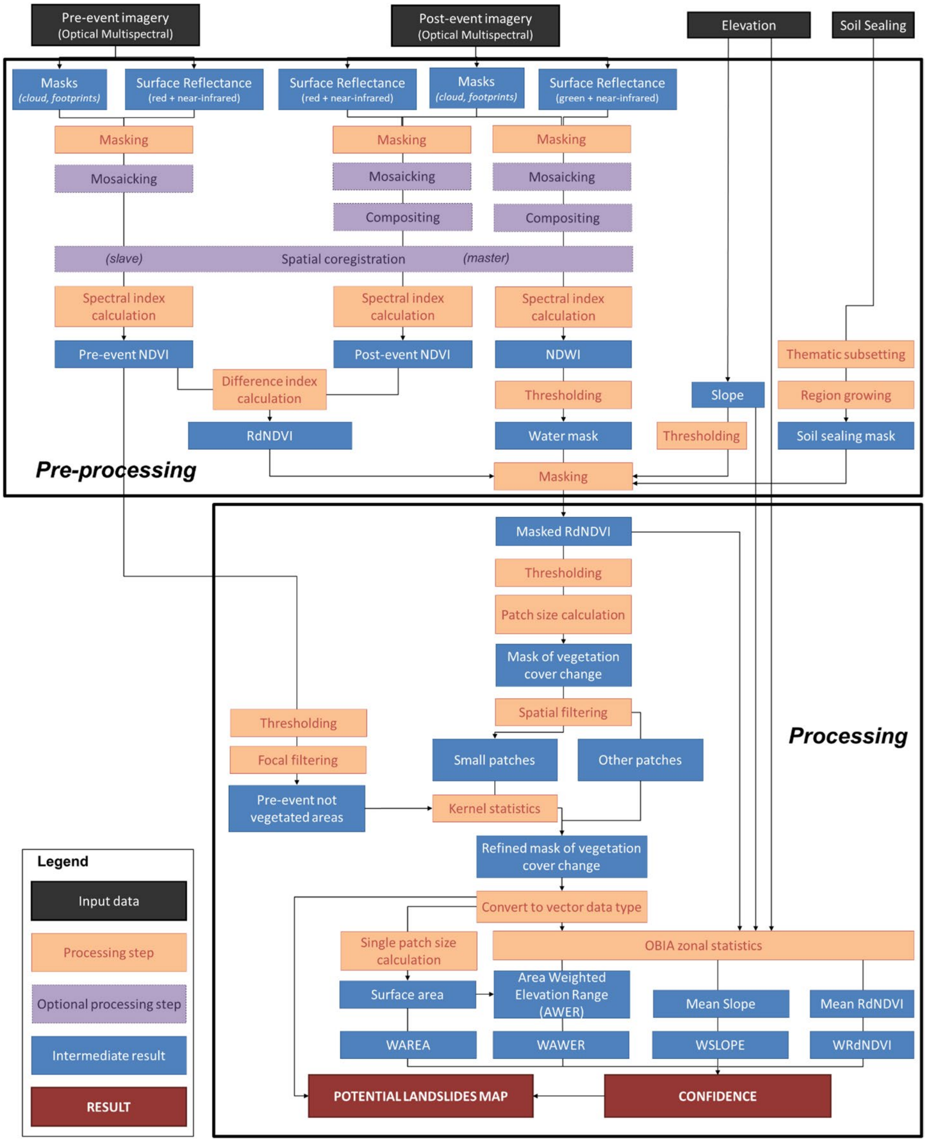

Fig. 2 Flowchart of the proposed procedure used to generate PL rapid mapping product

$$NDWI = \frac{(green - near\ infrared)}{(green + near\ infrared)} \tag{2}$$

For the selected case study, identified for development and testing of the procedure, pairs of satellite imagery acquired by MSI sensor onboard Sentinel-2 (S2) satellites constellation, and by SuperDOVE sensor onboard PlanetScope (PS) satellites constellation, were collected and analysed independently (Table 1). Selected spectral bands have a spatial resolution of 10 m in S2 acquisitions and 3 m spatial resolution in PS acquisitions. Ancillary

Table 1 Characteristics of input satellite data used for the analysis

Satellite	Sensor	Spatial resolution	Revisit time	Processing level used	Ancillary masks available	Pre-event acquisition dates (number of scenes)	Post-event number of scenes
Sentinel-2	MSI	10–20 m	5 days	L2A	yes	28/04/2023 (4)	23/05/2023 (4)
PlanetScope	SuperDOVE	3 m	1 day	L3B	yes	26/04/2023 (32) 27/04/2023 (46) 28/04/2023 (18)	17/06/2023 (39) 18/06/2023 (33)

masks provided with each satellite dataset were applied to selected spectral bands to mask out bad pixels from further analysis. Specifically, available masks of cloud pixels, cloud shadow pixels, topographic shadow pixels, and pixels outside the sensor acquisition footprint were used to mask out invalid pixels from S2 acquisitions. Available masks of cloud pixels were used to mask out invalid pixels from PS acquisitions. Mosaics of single masked spectral bands and pixel masks were generated and later used to produce one single post-event mosaic image and one single pre-event composite image for each satellite sensor.

4.2 Processing

Procedure for the identification of PL relies on the identification of changes related to vegetation cover decrease using a threshold value, which is followed by spatial filtering and the computation of a confidence measure.

First, the decrease in vegetation cover is identified by comparing post-event NDVI values with pre-event values, to obtain the Relative differenced Normalized Difference Vegetation Index (RdNDVI) (Eq. 3).

$$RdNDVI = \left(\frac{NDVI_{pre} - NDVI_{post}}{\sqrt{|NDVI_{pre}|}} \right) \tag{3}$$

where $NDVI_{pre}$ is the NDVI value in the pre-event raster and $NDVI_{post}$ is the NDVI value in the post-event raster.

Ancillary thematic mapping dataset is used to remove areas not prone to landslides from RdNDVI, specifically those having slope values lower than 3 degrees. Slope values are computed from digital elevation model. Furthermore, areas where a decrease in vegetation cover cannot be identified from remote sensing data, corresponding to water and sealed surfaces, are masked out from further analysis. A buffer of 10 m is applied to the sealed surfaces mask, in order to account for pixel contaminated by spatial proximity. Water areas are identified from NDWI spectral index computed from post-event satellite acquisitions, for NDWI values greater than 0.1. Mask is finally intersected with the AOI polygon and applied to RdNDVI.

Pixels corresponding to PL are identified by thresholding RdNDVI masked raster map. Each group of spatially connected pixels, referred to as a PL 'polygon' and representing the basic analysis unit in the OBIA approach, are identified with an image segmentation module based on the 4-connected neighbourhood.

Polygons with surface area smaller than a threshold value are removed from further analysis. Specifically, polygons with an area smaller than the threshold value are removed if they do not meet the requirement of being around an area with reduced vegetation cover in the pre-event phase. Such regions could be represented by landslide reactivation prone areas, with patchy distribution of vegetation cover in the pre-event phase, where it is necessary to maintain the identified small PL. Such areas are identified as those areas that report an NDVI value, calculated from the pre-event satellite acquisitions, less than 0.3 in at least 30% of the 3×3 kernel around each pixel.

Final processing step is the calculation of confidence measure, representing the level of confidence that the polygon is indeed a true landslide. Confidence value is calculated from a combination of weights, in the range 0–1, generated for 4 parameters related to slope, area, elevation range, RdNDVI. To this end, statistics on elevation, slope, surface area, RdNDVI, and patch metrics (e.g. patch shape index, fractal dimension index) are first calculated for each polygon, following an OBIA approach. Distribution of slope for previous landslides events, available from pre-event landslide inventories, can be exploited to assign the slope weight values (W_{SLOPE}) using a two parameters sigmoid function (Eq. 4), and to assign the area weight values (W_{AREA}) using a sigmoid function based on a four parameters Weibull distribution (type 2) (Eq. 5).

$$W_{SLOPE} = \frac{0.9979}{(1.0 + exp\,(a * (SLOPE - b)))} \tag{4}$$

where *a*, *b* are sigmoid function parameters, *SLOPE* is the slope value in degrees.

$$W_{AREA} = 1.095 - (c + (d - c) * exp(-exp\,(b * (log\,(AREA) - log\,(e)))) \tag{5}$$

where *b*, *c*, *d*, *e* are Weibull distribution parameters, *AREA* is the polygon surface area in m^2.

Weight of Area Weighted Elevation Range (W_{AWER}) is calculated according to Eq. 6:

$$W_{AWER} = tanh\left(\sqrt{0.1 + \frac{|(Z_{max} - Z_{min})|}{\sqrt{AREA}}}\right) \tag{6}$$

where Z_{max} is the maximum elevation value within the polygon, Z_{min} is the minimum elevation value within the polygon, *AREA* is the polygon surface area in $m.^2$

Weight of RdNDVI is calculated to according to Eq. 7:

$$W_{RdNDVI} = 3.0 * tanh\left(\sqrt{\frac{(RdNDVI - RdNDVI_{min})}{(RdNDVI_{max} - RdNDVI_{min})}}\right) \tag{7}$$

where *RdNDVI* is the RdNDVI pixel value, $RdNDVI_{min}$ is minimum RdNDVI raster value, $RdNDVI_{max}$ is maximum RdNDVI raster value.

Finally, confidence is calculated according to Eq. 8:

$$CONFIDENCE = \frac{(W_{SLOPE} + W_{AREA} + W_{AWER} + W_{RdNDVI})}{4} \tag{8}$$

where W_{SLOPE} is the weight referred to the polygon average slope, W_{AREA} is the weight referred to polygon area in m^2, W_{AWER} is the weight referred to area weighted elevation range, W_{RdNDVI} is the weight referred to RdNDVI. Considering all input parameters used in formulation, confidence measure will result in a value in the range 0–1.

For the selected case study, sealed surfaces were determined from Italian national land consumption map 2022 (Strollo et al. 2020; freely accessed at: https://groupware.sinanet.isprambiente.it/uso-copertura-e-consumo-di-suolo/library/consumo-di-suolo) at 10 m spatial resolution, specifically the classes coded 1, 11, 111, 114, 115, 116, 117, and 126 were considered to mask out pixels. NDWI threshold value to mask out water pixels was set to 0.1. Digital elevation model used for the analysis is the TIN Italy product. Slope threshold value used for masking RdNDVI was set to 3.0. The threshold value on RdNDVI was defined through visual interpretation of several hundred PL identified from S2 acquisitions. In order to generate comparable results from the analysis of S2 and PS data, RdNDVI threshold used for PS analysis (RdNDVI > 0.173) was derived from linear regression analysis with the selected threshold used for S2 (RdNDVI > 0.2). With respect to small area threshold, tested values are: 0 m^2 (no filtering); 200 m^2; 400 m^2. IFFI Inventory was used to calculate the distribution of slope and areas for previous landslides events, that were later exploited to assign the slope (W_{SLOPE}) and area (W_{AREA}) weight values.

The procedure for rapid mapping of PL, described in this processing phase section, was fully automated through a bash script and makes use of GDAL library, R programming languages and the related 'sf' (Pebesma 2018) and 'terra' (Pebesma and Bivand 2023) libraries. Script can be freely accessed at: https://github.com/ffilipponi/LandslidesRapidMapping.

4.3 Post-processing

Post-processing steps aims at generating operational PL rapid mapping products and statistics, to support response in case of emergency activations.

PL density distribution map was generated at 1 km spatial resolution by spatially downscaling the PL rapid mapping products at their original spatial resolution (S2: 10 m; PS: 3 m). Spatial overlay of PL rapid mapping polygons with the road and railway networks, collected from OpenStreetMap (https://www.openstreetmap.org), was done to assess the potential impact of the event on the civil infrastructures. A buffer distance of 10 m was applied to road and railway networks prior the overlay analysis. Number of spatial intersections was calculated, excluding road and railway segments in tunnels and on bridges. A spatial grid at 1 km spatial resolution, the same used for generating PL density distribution map, was utilized to calculate km of roads potentially intersecting the PL within each cell.

Classification performance of the proposed methodological approach was assessed by comparing mapped PL to reference event inventories (Ferrario event inventory; ER region event inventory). Validation procedure was performed following a raster-based approach, based on polygon surface area and accounting for pixel fractional coverage in the conversion of vector polygons to raster. Classification performance metrics were calculated for each confidence level in the range 0–1 with a step size of 0.01. Confusion matrices were generated to report surface area of the following types: true positive (TP), identified as landslides in both rapid mapping and reference event inventory; false positive (FP), identified as landslides in rapid mapping product and not overlaying any of the polygons in reference event inventory; true negative (TN), the areas not corresponding to landslides in both rapid mapping and reference event inventory; and false negative (FN), corresponding to areas not identified by rapid mapping but mapped as landslides in reference event inventory. Confusion matrices enable the subsequent calculation of the classification performance metrics for binary cases, including: accuracy, precision, False Detection Rate (FDR), True Positive Rate (TPR), False Positive Rate (FPR), False Negative Rate (FNR). The supplementary uncommon Jaccard similarity coefficient, also referred to as Intersection over Union (IoU), providing an estimate of the similarity between corresponding classes in two different mapping products (Fiorucci et al. 2018), was also calculated. In addition, validation through the comparison of number of mapped polygons was done. Furthermore, a check of the model outputs was carried out on some landslide sites documented with post-event photos and videos.

4.4 Statistics analysis

The distribution of land use classes in the AOI was compared against Ferrario event inventory, in the TP, FP and FN landslides polygons. For this purpose, a detailed land use layer was generated for the AOI with Corine Land Cover (CLC) level 3 classification by mosaicking the land use data of ER Region 2020 at scale 1:10,000, of Tuscany Region 2019 at scale 1:10,000. For the portion of the AOI falling within the Marche Region, CLC 2018 at scale 1:100,000 was used, as the regional data is classified only at CLC level 2. The relative landslide index (Eq. 9) has been processed to assess the relative importance of each land use class with respect to landsliding (Subscript *i* indicates the i-th land use class; Lee and Min 2001; Trigila et al. 2015):

$$IFrel = \frac{\frac{landslidearea_i}{landslidearea_{tot}}}{\frac{nolandslidearea_i}{nolandslidearea_{tot}}} \tag{9}$$

An analysis of areas identified by rapid mapping as PL on S2 and PS imagery was performed with respect to the landslides mapped in the two reference events inventories and to the pre-event IFFI Inventory. In particular, the cumulative frequency distribution of the polygon areas and the frequency distribution of the mean slope angle were compared.

Additionally, the percentage of newly formed landslides compared to reactivations in areas already affected by landslides in the past was investigated. Comparing the landslide event and the geomorphological historical inventories allows to ascertain landslide spatial persistence, that is the degree to which new slope failures occur in the same place as existing landslides (Guzzetti et al. 2012).

4.5 Cumulative rainfall data interpolation

To compare the density of landslides occurred in the AOI with the spatial patterns of rainfall, a detailed raster map of cumulative precipitation for the events has been produced. Rainfall measurement points, acquired from May 1, 2023, to May 17, 2023, and including the two events, were provided and validated by the bulletins of the ER region environmental agency (ARPAE). All measurements points were georeferenced and interpolated using the kriging method in QGIS, to create a spatial distribution of cumulative rainfall occurred during the events.

5 Results

Small area threshold sensitivity analysis done from S2 imagery revealed that using a threshold value of 200 m^2, 54.97% of polygons smaller than the threshold value were removed, corresponding to 86.21% of total mapped polygons without the use of a threshold on polygon size (i.e. small area threshold equal 0 m^2). While removing 45.80% of FP polygons, 9.18% of TP polygons were removed, corresponding to a total area of 0.7032 km^2 (0.3675% of the overall mapped landslides area). By applying a small area threshold value of 400 m^2, 84.08% of polygons smaller than the threshold value were removed, corresponding to 33.88% of total mapped polygons without the use of a threshold on polygon size. While removing 29.40% of FP polygons, 4.48% of TP polygons were removed, corresponding to a total area of 2.4774 km^2 (1.2947% of the overall mapped landslides area). Based on these results, small area threshold used for mapping landslides was set to 400 m^2, in order to balance the omission and commission errors, and to optimize the removal of FP.

The following values, calibrated from pre-event IFFI Inventory, were used as parameters in Eq. 4: $a=-0.7859$; $b=10.9374$ and in Eq. 5: $b=-1.4058$; $c=1.0950$; $d=0.9986$; $e=6{,}947.7772$.

Results obtained from the comparison of PL rapid mapping products and reference event inventories for various confidence levels, through the calculation of classification performance metrics, are shown in Fig. 3. Based on the performance metrics, confidence values of 0.3, 0.5 and 0.7 were selected. From the comparison with reference event inventories, the use of a confidence threshold value of 0.7 can optimize the accuracy of the PL mapping product generated from both S2 and PS imagery, representing a trade-off between the number of commission (i.e. FP) and omission (i.e. FN) errors. This can be effectively demonstrated by the trajectory of IoU similarity coefficient, rather than by single false positive and false negative detection rates (Fig. 3).

The results for the accuracy metrics using various weights sets are presented in the supplementary material Fig. S2. The statistical results for the comparison of RdNDVI and dNDVI mapping performances are presented in the supplementary material Fig. S3.

Figure 4 shows the landslides density distribution, calculated for cells of 1 km^2 size from reference event inventories and the PL rapid mapping products generated from S2 and PS imagery, applying various confidence threshold values.

As shown in Tables 2 and 3, the PL rapid mapping product performance improves by increasing the confidence value from 0.3 to 0.7: in fact, the TP increase, the FP are significantly reduced and the increase in FN remains, however, limited. Taking into account that the ER region event inventory has a higher number of landslides polygons (and landslides total area) than the inventory released shortly after the event in June 2023 (Ferrario event inventory), the rapid mapping validation results show a higher value of TP, lower FP, and higher FN using the ER region event inventory as a reference.

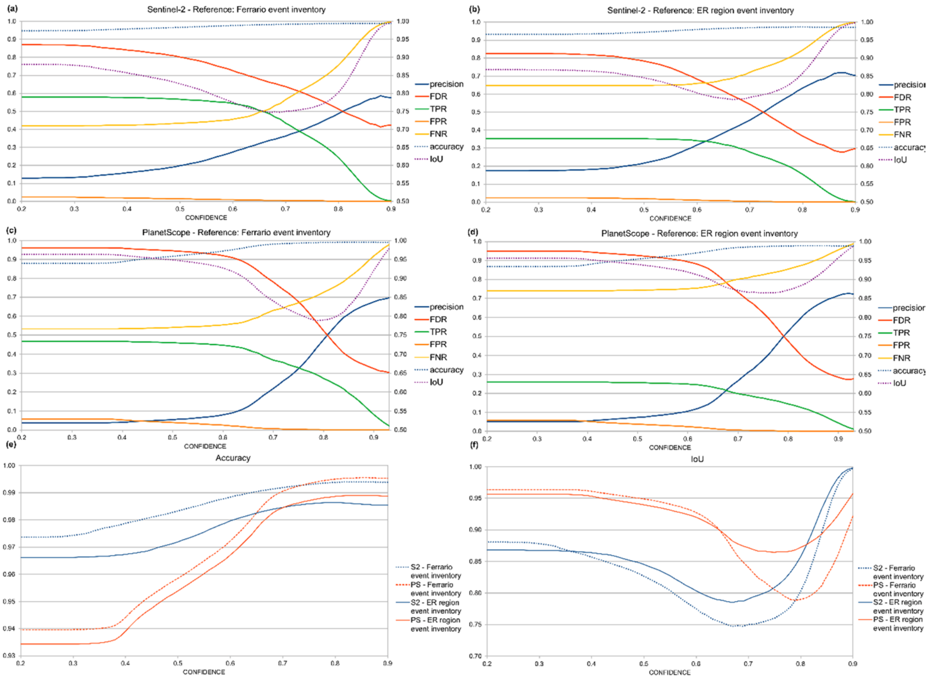

Fig. 3 Classification performance metrics for various confidence levels; plots refer to Sentinel-2 (**a**–**b**) and PlanetScope (**c**–**d**) data, considering the Ferrario and ER event inventories. Plots e and f show the variation of accuracy and Intersection over Union as a function of increasing confidence

The comparison with reference event inventories performed on a vector base (PL represented by polygon features) allowed to establish the reliability of the PL rapid mapping procedure: rapid mapping procedure was able to detect 63,944 PL from S2 and 142,967 PL from PS. As summarized in Table 2, rapid mapping from PS detected 20.1% of occurred landslides (TP), while the 79.9% were FP, mainly agricultural fields probably managed in the time span from pre- and post-event NDVI PS mosaics. When a confidence threshold value greater than 0.7 is considered, mapping from PS detected 40.0% of occurred landslides (TP) and 60.0% of FP. Analogously rapid mapping from S2 detected 28.5% of occurred landslides (TP), while the 71.5% were FP. When a confidence threshold value greater than 0.7 is considered, mapping from S2 detected 55.3% of occurred landslides (TP) and 44.7% of FP.

The cumulative frequency distribution of the landslide area and the distribution of the mean slope angle highlight the difference of the May 2023 event compared to the pre-event IFFI Inventory (Fig. 5). While in the latter, considering all types of movement (mainly slides, slow earth flows and complex landslides), 42.4% of landslides have an area between 1,000 and 10,000 m^2 and 47.1% between 10,000 and 100,000 m^2, in the two reference event inventories the percentage of landslides with an area less than 1,000 m^2 is respectively 77.8% (Ferrario event inventory) and 74.1% (ER region event inventory) and is 49% and 43.5% below 400 m^2. The distribution of the mean slope in the polygons of the pre-event IFFI Inventory shows a peak value at 15° and almost 92% of the landslides with values between 8 and 26° of mean slope. In the May 2023 Event Inventories, the peak is at 22–24°

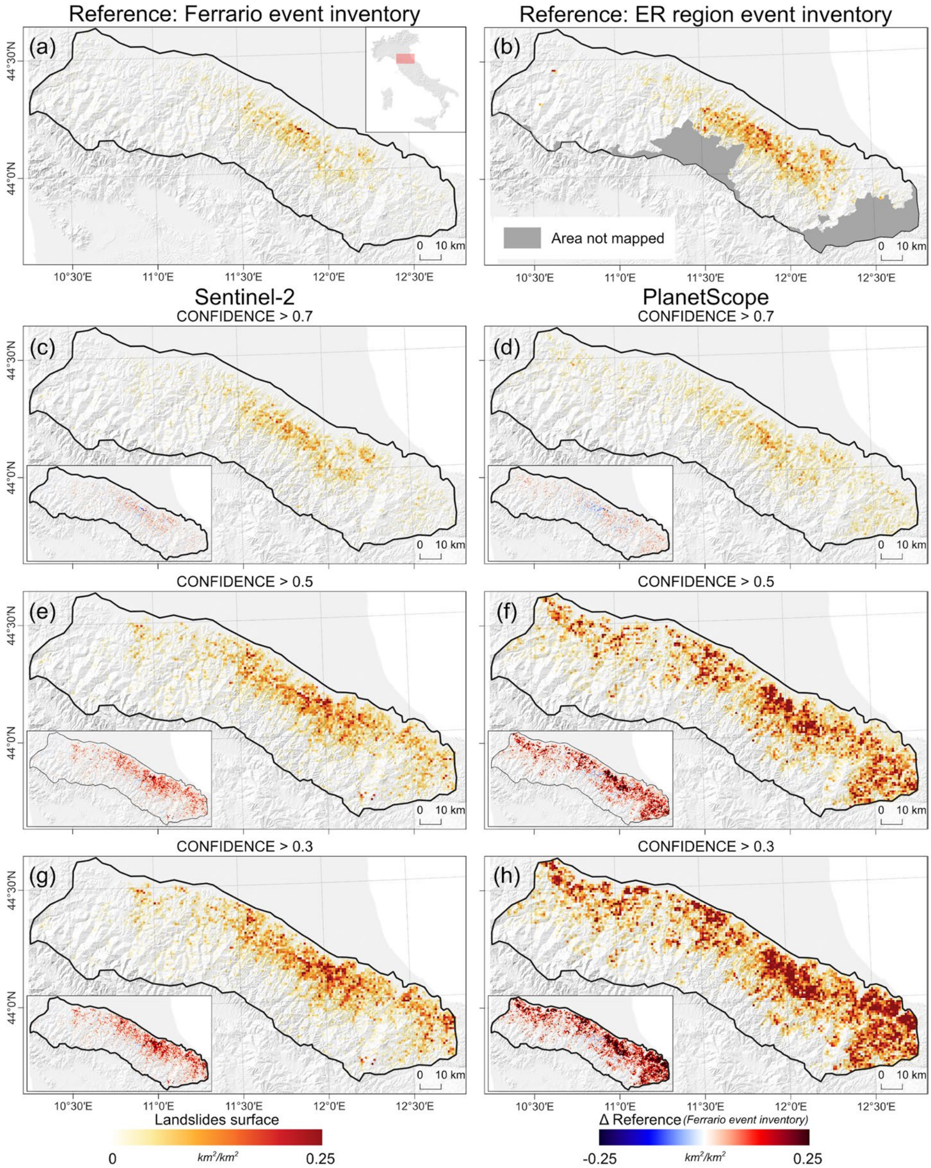

Fig. 4 Maps of landslide density distribution for the reference event inventories (**a**: Ferrario; **b**: ER event inventory) and PL rapid mapping products (**c**: Sentinel-2 data at confidence > 0.7; **d**: PlanetScope data at confidence > 0.7; **e**: Sentinel-2 data at confidence > 0.5; **f**: PlanetScope data at confidence > 0.5; **g**: Sentinel-2 data at confidence > 0.3; **h**: PlanetScope data at confidence > 0.3)

and the distribution has a greater dispersion with more than 91% of the landslides with values between 10 and 40° of mean slope. The analysis of other events that occurred worldwide suggests that exceptional/extreme rainfall events trigger mostly shallow and rapid moving landslides, mainly due to a high water availability inducing a rapid increase in water content and pore pressure and loss of matric suction in the first soil horizons, not necessarily

Table 2 Summary of PL identified by the proposed rapid mapping procedure (at confidence threshold values greater than: 0.0, 0.3, 0.5, 0.7) from Sentinel-2 (S2) and PlanetScope (PS), compared against Ferrario event inventory over the full AOI: Total mapped PL, True Positive (TP), False Positive (FP), False Negative (FN)

	Total mapped PL		True Positive (TP)		False Positive (FP)		False Negative (FN)	
	No. polygons	Area (km^2)	No. polygons	Area (km^2)	No. polygons	Area (km^2)	No. polygons	Area (km^2)
S2—conf. > 0.0	63,944	176.94	18,196 (28.5%)	22.99 (13.0%)	45,748 (71.5%)	153.95 (87.0%)	25.599 (52.1%)	19.46 (45.8%)
S2—conf. > 0.3	63,934	176.56	18,196 (28.5%)	22.99 (13.0%)	45,738 (71.5%)	153.58 (87.0%)	25.599 (52.1%)	19.46 (45.8%)
S2—conf. > 0.5	58,525	141.66	18,125 (31.0%)	22.83 (16.1%)	40,400 (69.0%)	118.83 (83.9%)	25.697 (52.3%)	19.61 (46.2%)
S2—conf. > 0.7	29,659	50.96	**16,415 (55.3%)**	**17.58 (34.5%)**	**13,244 (44.7%)**	**33.39 (65.5%)**	**28.879 (58.8%)**	**24.87 (58.6%)**
PS—conf. > 0.0	142,967	515.69	28,746 (20.1%)	19.50 (3.8%)	114,221 (79.9%)	496.19 (96.2%)	20.160 (41.1%)	22.94 (54.0%)
PS—conf. > 0.3	142,961	515.49	28,746 (20.1%)	19.50 (3.8%)	114,215 (79.9%)	495.98 (96.2%)	20.160 (41.1%)	22.94 (54.0%)
PS—conf. > 0.5	117,880	352.31	28,315 (24.0%)	19.16 (5.4%)	89,565 (76.0%)	333.15 (94.6%)	20.557 (41.9%)	23.28 (54.9%)
PS—conf. > 0.7	64,832	70.24	**25,906 (40.0%)**	**15.41 (21.9%)**	**38,926 (60.0%)**	**54.83 (78.1%)**	**23.942 (48.8%)**	**27.03 (63.7%)**

AOI total area: 8,981 km^2; Ferrario event inventory: 49,101 polygons; area 42.4 km^2. The values in parentheses represent the percentage relative to the total mapped positives (True Positive and False Positive columns), and relative to the Ferrario event inventory (False Negative columns). The percentages obtained with a confidence threshold of 0.7 were emphasized in "bold", as this threshold demonstrated the highest reliability during validation

linked to peculiar flow accumulation patterns, as Marche-Umbria 2022 event and Sicily 2009 events (Donnini et al. 2023).

Effects of the spatial resolution of source imagery are visible from curves in Fig. 5a, highlighting the lower capabilities in the detection of small patches. Comparing the two PL rapid mapping products, 92.4% of the polygons identified from S2 imagery as PL, with a confidence value > 0.7, have an area > = 500 m^2; instead, 63.4% of the polygons identified from PS imagery have an area < 500 m^2. With respect to the mean slope distribution, the rapid mapping on S2 identifies more polygons with a mean slope angle greater than 20° compared to PS; polygons identified by PlanetScope with mean slope angle lower than 20 degrees are mainly false positives in arable land.

The comparison with the pre-event IFFI inventory highlighted that just over 1/5 of the landslide area of the 2 reference event inventories is a reactivation of portions of existing landslides, while almost 4/5 of the area are newly formed landslides. Comparable percentages are found in PL rapid mapping products (see supplementary material Table S1).

5.1 Analysis of landslides occurrence compared to cumulative rainfall

The landslides reference event inventories show a good correlation between the landslides surfaces density and areas with the maximum cumulative rainfall. Centroids spatial distribution analysis has shown that landslides are mainly concentrated on the central/north-eastern part of the AOI, in correspondence with the highest cumulative rainfall values area (Fig. 6a)

Table 3 Summary of PL identified by the proposed rapid mapping procedure (at confidence threshold values greater than: 0.0, 0.3, 0.5, 0.7) from Sentinel-2 (S2) and PlanetScope (PS), compared against ER region event inventory over the ER region territory intersecting the AOI: Total mapped PL, True Positive (TP), False Positive (FP), False Negative (FN)

	Total mapped PL		True Positive TP		False Positive FP		False Negative FN	
	No. polygons	Area (km^2)	No. polygons	Area (km^2)	No. polygons	Area (km^2)	No. polygons	Area (km^2)
S2—conf. > 0.0	56,564	157.31	19,166 (33.9%)	27.52 (17.5%)	37,398 (66.1%)	129.79 (82.5%)	48,894 (61.0%)	55.81 (67.0%)
S2—conf. > 0.3	56,554	156.94	19,166 (33.9%)	27.52 (17.5%)	37,388 (66.1%)	129.41 (82.5%)	48,894 (61.0%)	55.81 (67.0%)
S2—conf. > 0.5	51,848	126.58	19,090 (36.8%)	27.45 (21.7%)	32,758 (63.2%)	99.12 (78.3%)	49,044 (61.2%)	55.88 (67.1%)
S2—conf. > 0.7	27,461	47.63	**17,191 (62.6%)**	**21.74 (45.7%)**	**10,270 (37.4%)**	**25.88 (54.3%)**	**53,346 (66.5%)**	**61.59 (73.9%)**
PS—conf. > 0.0	123,862	428.54	32,444 (26.2%)	22.56 (5.3%)	91,418 (73.8%)	405.98 (94.7%)	42,892 (53.5%)	60.78 (72.9%)
PS—conf. > 0.3	123,857	428.35	32,444 (26.2%)	22.56 (5.3%)	91,413 (73.8%)	405.79 (94.7%)	42,892 (53.5%)	60.78 (72.9%)
PS—conf. > 0.5	102,800	288.98	32,071 (31.2%)	22.30 (7.7%)	70,729 (68.8%)	266.68 (92.3%)	43,312 (54.0%)	61.04 (73.2%)
PS—conf. > 0.7	58,625	61.35	**29,326 (50.0%)**	**17.38 (28.3%)**	**29,299 (50.0%)**	**43.97 (71.7%)**	**48,555 (60.5%)**	**65.95 (79.1%)**

AOI area within ER region: 7,440.9 km^2; ER region event inventory: 80,194 polygons; area 83.3 km^2. The values in parentheses represent the percentage relative to the total mapped positives (True Positive and False Positive columns), and the percentage relative to the ER region event inventory (False Negative columns). The percentages obtained with a confidence threshold of 0.7 were emphasized in "bold", as this threshold demonstrated the highest reliability during validation

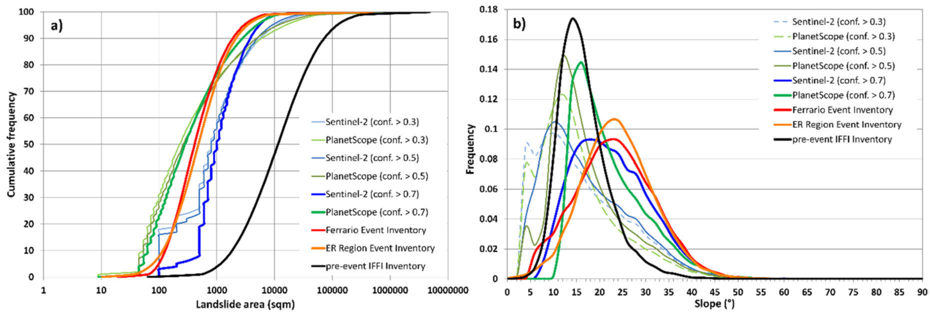

Fig. 5 **a** Cumulative frequency distribution of the landslide area and **b** the distribution of the mean slope angle for: pre-event IFFI Inventory; two reference event inventories realized manually; PL rapid mapping products generated from S2 and PS at 3 confidence values (0.3, 0.5, 0.7)

and confirmed by the governmental official reports (Arpae-SIMC 2023d) as well as the in-situ surveys.

The rapid mapping of S2 and particularly PS produced a higher number of PL polygons with respect to reference event inventories. It follows that the less refined data (with confidence of 0.3 and 0.5) appears too scattered to show an exact correlation with the precipitations, although there is still a high density of landslides in those areas with high cumulative rainfall. However, another issue concerns the 0.7 confidence level, where it is possible to

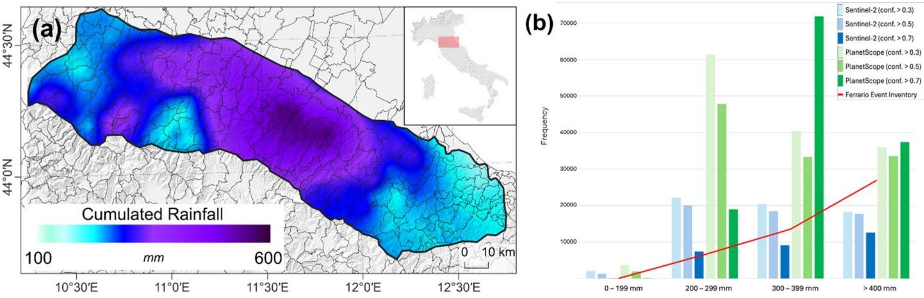

Fig. 6 **a** Interpolated cumulative rainfall map for the events; **b** Frequency values of Ferrario event inventory and PL rapid mapping products generated from S2 and PS at 3 confidence values (0.3, 0.5, 0.7) for 4 cumulative rainfall classes

establish an exact correlation between the highest density of landslide affected area and the maximum cumulative rainfall.

The highest frequency values of PL are included at precipitation values higher than 300 mm both for S2 and PS (Fig. 6b). Spatial comparison between rapid mapping and reference event inventories confirmed also the good reliability of 0.7 confidence, showing on average PL values closer to the reference ones for all ranges of cumulative rainfall.

5.2 Analysis of land use classes

Comparing the distribution of land use classes in the AOI and in the Ferrario event inventory, it emerges that the land use classes with a relative landslide index greater than 1, which denotes a direct correlation with landslide, are Areas with sparse vegetation (IFrel 6.6), the Olive groves (IFrel 2.4), the Areas with sclerophyllous vegetation (IFrel 1.8).

The distribution of land use classes in the TP areas, identified by PL rapid mapping from S2 (17.6 km^2) and PS (15.4 km^2) imagery, is comparable with that of the Ferrario event inventory (Fig. 7). As regards the FP areas, identified by rapid mapping but not contained in the reference polygons (S2 33.4 km^2; PS 54.8 km^2), the predominance of non-irrigated arable land areas emerges in the case of PS (64% of the FP surface); 6% of FP areas instead are reported in the watercourse class for S2. Percentage of FN, TP, and FP for the main land use for S2 and PS polygon areas are shown in supplementary material Fig. S4.

The risk analysis on the railway line, buffered at 10 m, highlighted that the infrastructure mainly affected by the May, 2023 event was the Faentina railway; the critical points of landslides intersecting the railway network amount to 16 using the ER region event inventory, 15 with the Ferrario event inventory, 6 considering the PL areas identified by the rapid mapping on PS acquisitions and 19 on S2 acquisitions (confidence > 0.7). The intersections along the road network are several thousand (12,431 with ER region event inventory, 6,981 with Ferrario event inventory, 9,674 with PS and 5,642 with S2). In 95% of cases, the intersections involve tertiary, minor (e.g. residential, cycleway) or not classified roads. The density distribution of potentially affected road network on the 1 km grid showed maximums up to 500 m of road per km^2 in some municipalities of the provinces of Ravenna and Forlì-Cesena (Fig. 8).

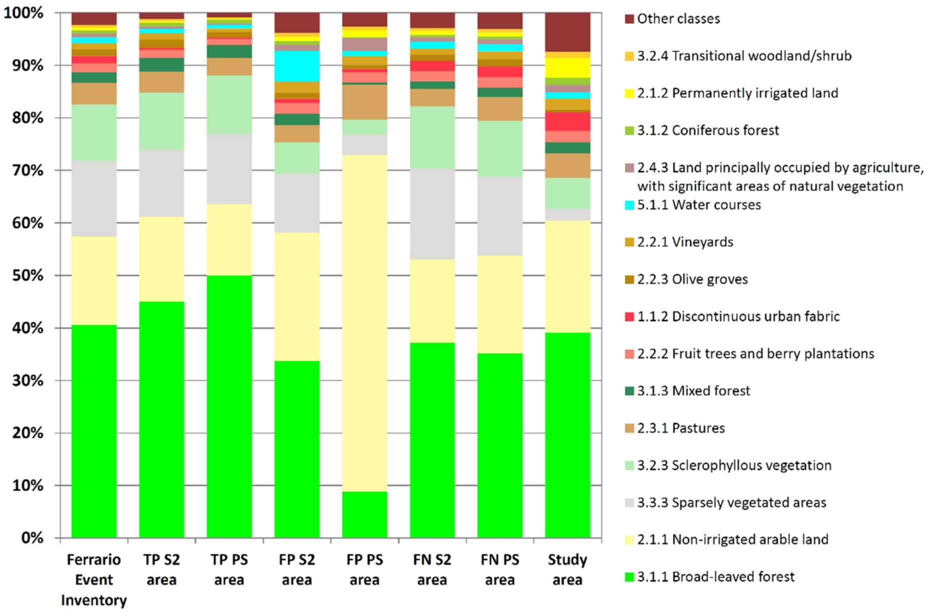

Fig. 7 Distribution of land use classes in the study area, in the Ferrario Event Landslide Inventory, in the TP areas identified by rapid mapping on S2 and PS, in the FP areas and in the FN areas

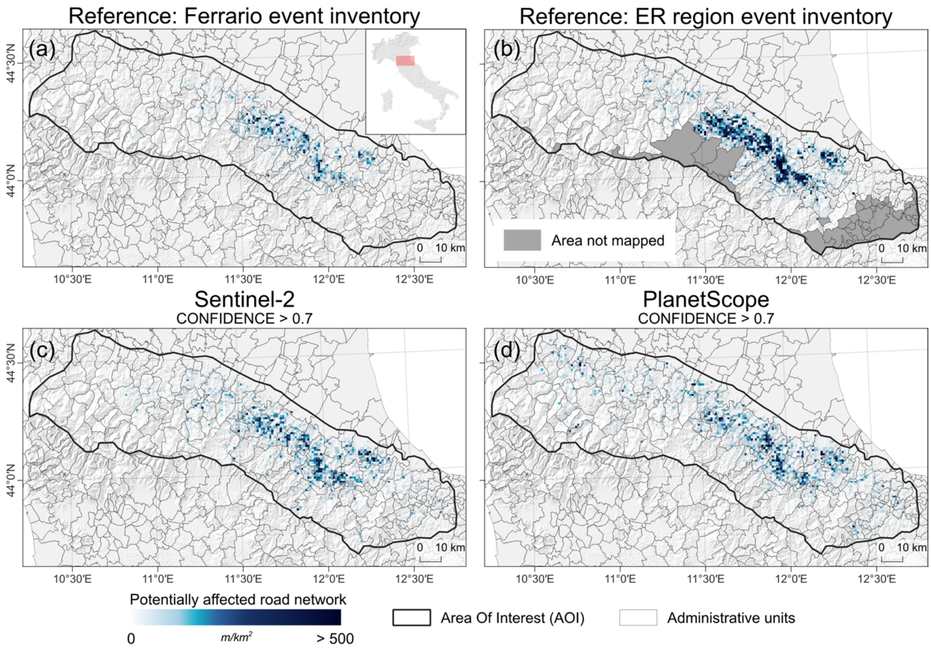

Fig. 8 Density distribution of potentially affected road network by landslides for reference event inventories and PL rapid mapping products generated from S2 and PS at confidence > 0.7

6 Discussion

Use of remote sensing data to support landslides mapping and populate landslides inventories has been already demonstrated in literature (Mondini et al. 2011; Prakash et al. 2021; Uehara et al. 2022; Notti et al. 2023; Satriano et al. 2023). Most of all, the aerial and satellite acquisitions allow to quantify changes in spatial and temporal dimensions and thus enable ex-post assessment of pre-event conditions. The availability of Copernicus Sentinel-1 and S2 data in recent years, distributed with open access policy, resulted in a 600% increase in the number of papers related to landslide mapping from satellite remote sensing imagery after year 2014 (Novellino et al. 2024). Rapid mapping of PL specifically aims to generate a prompt reliable mapping product as soon as satellite or aerial acquisitions are available. Generation of PL rapid mapping products and statistics can support effective and efficient response in case of emergency activations. Statistical analysis on administrative units, as well as identification of potential number of affected infrastructures (e.g. roads, railways), can provide useful information to prioritize the interventions to be addressed in emergency response.

The approach here proposed to generate PL rapid mapping product relies on change detection analysis of the vegetation cover using a simple spectral index, calculated from optical multispectral imagery. The choice to select a simple spectral index is motivated by the aim of maximizing the application of the proposed procedure to many sensors onboard satellites and aerial vehicles, including UAS. Among the various spectral indices that are proxies for photosynthetically active vegetation cover, NDVI was selected because of: (i) the index formulation uses the spectral bands in the red and near-infrared radiometric ranges, which are typically available in both high and very-high resolution optical multispectral sensors, making the methodology applicable to a wide number of remote sensing datasets; (ii) red and near-infrared spectral bands, unlike those in other radiometric ranges such as shortwave infrared and red-edge, are available at higher spatial resolution in S2 MSI satellite acquisitions; (iii) in contrast to other vegetation indices (e.g. kNDVI, NIRv), the saturation effect of NDVI (Filipponi et al. 2022) allows for greater sensitivity to changes in vegetation cover, for cases of pre-event reduced vegetation cover conditions. To further reduce the omission error, RdNDVI was selected in place of the difference NDVI (dNDVI), that is widely used in literature (Notti et al. 2024). As compared to dNDVI formulation, which is the arithmetic difference between post-event and pre-event NDVI values, the use of the relative difference in time of NDVI (RdNDVI) allows to better account for low vegetation cover status before event, a condition that may occur for example in gullies when high resolution imagery is used. The use of an approach based on relative difference in time was inspired by the implementation of the RdNBR spectral index, whose operating principle allows a better discrimination of burnt scars in area with low vegetation cover (Miller and Thode 2007). Numerical results from the comparison of RdNDVI against dNDVI demonstrate that RdNDVI reaches a better accuracy than dNDVI in PL rapid mapping from both S2 and PS imagery (see supplementary material Fig. S2). The identification of a single threshold value, which could be globally valid, to be used for the detection of PL from RdDNVI, remains one of the main problems still without solution in this and other applications.

Considering the high rate of landslides FP generated using semi-automatic classification approaches using change detection or artificial intelligence, a strategy is needed to account for such limitations and allow the effective use of rapid mapping products. In addition to the implemented data masking and spatial filtering techniques, like the use of a threshold value on slope (Vecchiotti et al. 2021) and NDWI, the inclusion of a confidence measure is proposed here as a solution to optimize the accuracy of the mapping product, representing a trade-off between the number of commission (i.e. FP) and omission (i.e. FN) errors generated. Calculation of a confidence measure for each generated PL polygon is hence one of the strengths of the approach, introducing the OBIA technique. The possibility to consider individual polygons based on their confidence value, or to use a confidence value threshold for generating different scenarios of the distribution of landslide-affected areas, as well as the use of a single or multiple combinations of ancillary quantitative information provided for each polygon, is left to expert operators exploiting the PL rapid mapping product.

The approach used for confidence calculation allows to combine OBIA with pixel-based image analysis used in previous processing steps. The selected parameters come from statistical analysis of the distribution of variables related to patch metrics, polygon shape (e.g. ellipses), other than those finally selected and related to slope, surface area, elevation range and RdNDVI (not shown). According to confidence formulation (Eq. 8), polygons with steep slopes, small surface area, large elevation range, and high RdNDVI values can likely result in high values of the confidence measure. Distribution functions, particularly those used to assign weights based on slope (W_{SLOPE}) and surface area (W_{AREA}), can be tuned using statistics based on local landslides inventory, when available. Also, definition of different function types is possible. The distribution function of slope values must also take into account that low slope values, representing areas of accumulation, contribute to lowering the average slope value referred to each polygon. Comparison of various sets of weights used to compute confidence, using the Leave-One-Out statistical approach, shows that the combination of the full set of 4 weights achieves generally better performance (see supplementary material Fig. S2).

The use of reference event inventories, consisting of landslides mapping products as vector representations, allowed to establish how reliable and precise the PL rapid mapping product is at different confidence values. Three confidence threshold values were selected to produce PL density distribution maps and generating three different scenarios for which further statistical analyses were performed. Based on the classification performance metrics, with a specific focus on the IoU, confidence threshold value of 0.7 was selected as the most conservative scenario.

Advanced spatial filtering approach to remove the detected polygons with small surface area was developed, which considers the presence of low or patchy distribution of pre-event vegetation cover using focal filtering, that is typically the case in areas where landslides reactivation or extension processes occur. The use of spatial filtering, specifically designed to account for areas with patchy distribution of vegetation cover, allowed to effectively reduce number of FP polygons while minimize the number of TP polygons removed. Considering that FP is composed of a huge number of very small polygons, most of them smaller than the selected small area threshold of 400 m^2, the developed spatial filtering criteria offers a good trade-off to optimize accuracy.

The proposed processing procedure only needs a small number of input datasets, namely digital elevation model, pre-event NDVI, post-event NDVI and NDWI indices, to produce PL rapid mapping product. Although fully automated, it allows the operator to set key parameters to be used for data analysis (i.e. RdNDVI threshold for the detection, small area threshold). In addition, the operator can provide a spatial polygon and custom raster mask to define the geographical area to be analyzed. The use of combined qualitative thematic information provided by the operator (e.g. a soil sealing mask derived from land cover thematic mapping products), derived from DEM (using a threshold value on slope) and generated from selected ancillary information of each satellite acquisition (e.g. clouds, cloud cover, water areas), has the scope to reduce the commission error.

As regards the pre-processing phase, radiometric topographic correction should be considered, when not yet applied in the collected datasets, especially for cases of large time spawn between pre-event and post-event imagery acquisition dates. Further, the use of a spatial co-registration algorithm at the end of the pre-processing phase could minimize the effect of spatial misalignment of pre-event and post-event acquisitions (Filipponi, in press), possibly reducing biases in subsequent processing steps for change detection analysis. The use of information contained in NDWI allows to remove areas corresponding to a decrease in vegetation cover in the considered time interval due to factors other than landslides, such as flooding areas with a residual clay deposit.

At the time of writing, two manually mapped landslides event inventories were published with open-access policy (i.e., Ferrario event inventory and ER region event inventory, see Sect. 3). These inventories are relevant assets for providing a reference upon which to evaluate PL rapid mapping product performance. The two reference event inventories have different area coverage and were released at different times. Here, we used the Ferrario event inventory, updated to cover the whole AOI, as the main reference because it was made available with open-access distribution policy few weeks after the triggering events (published on the Zenodo repository on June 28, 2023), while the ER region event inventory was released much later. The selected main reference landslides event inventory was realized from 3 m resolution PS imagery, which was exploited also here using fully automated procedure.

Dealing with different spatial data types, namely reference event inventories as vector representations and PL rapid mapping products as raster representations, the comparison of the mapping products on a vector basis can be critical, due to topological errors generated in the conversion from raster to vector. To maintain the spatial details of each mapping product as much as possible, validation procedure was also performed following a raster-based approach, accounting for pixel fractional coverage in the conversion of vector polygons to raster. This approach allows to also calculate TN and FN surface areas, together with derived error metrics. Validation through the comparison of the number of mapped polygons can result in biases due to the partial polygons intersection, as well as to the fragmentation of a single landslide area into multiple polygons that sometimes is exhibited in the PL rapid mapping. The use of the 4-connected neighborhood used to convert raster binary map to vector polygons is likely one of the causes for increased fragmentation of the landslides spatial representation, which results in a greater number of single polygons.

S2 mapped area, not masked during pre-processing phase is about 72.1% of the AOI, while PS mapped area is about 95.6% of the AOI. Such difference is partly due to the higher efficacy of PS pre-event composite, that is related to higher probability of sensing Earth surface without cloud cover in a short time interval, thanks to daily revisit capacity of the PS satellites constellation. Several FP polygons with high surface area were found in areas that were likely undergoing agricultural practices such as ploughing and tillage. The use of a time interval as short as possible between pre-event and post-event acquisitions, can play a key role in reducing the changes in vegetation cover caused by factors other than landslides.

In general, mapping from S2 imagery resulted in a higher accuracy as compared to mapping from PS imagery. Increase of confidence threshold value to 0.7 allowed to significantly increase TP area mapped, while decreasing the FP areas. While high confidence value can reduce FP polygons, threshold value should be selected with caution, since very high confidence values (closer to 1) may cause a significant increase of FN areas.

Considering that a sealed surfaces mask was adopted as input in the rapid mapping model, the risk analysis relating to buildings was not performed as it would have led to a significant underestimation. However, risk analysis on the railway and road network revealed several thousand of potential intersections.

A qualitative analysis of the classified RdNDVI raster allowed to distinguish all NDVI variations in the time span of the pre-event NDVI and the post-event NDVI, of which most were landslides; however, this procedure detected as FP managed agricultural fields and river scarp erosion. RdNDVI classified raster also clearly shown the landslides morphologies, when compared to recent Google Earth images (Google Earth images July 2023).

From the comparison with reference event inventories and recent Google Earth satellite images, landslides shapes are well identified from the PS rapid mapping, in most cases. In the details examples of Figs. 9 and 10 is clearly shown the valuable landslides morphological relevance detection, identified with longitudinal evolution along the hillslope, typical of complex earth-slide (Cruden and Varnes 1996).

In addition to new landslides activations, several reactivations were also identified, for example in gullies areas (Fig. 11): before the event gullies were partially covered by grass (Fig. 11c and e), after the event there was the reactivation of gullies erosion (Fig. 11d and f).

The analysis performed on some case studies, documented with post-event photos and videos, through comparison of the PL rapid mapping and the two reference event inventories, has highlighted:

- the presence of FP, especially in areas characterized by hyperconcentrated flows (e.g. Fig. 9a, 9b and 9c), or in arable zones (e.g. Figs. 9c and 10a);
- the presence of some FN, in case of small size landslides in vegetated areas (broadleaved forests), or on the riverbanks (e.g. Fig. 10c and d);
- the presence of FN in areas affected by event landslides with spatial continuity, because the polygons resulting from rapid mapping have a very large area (>7.2 ha) and confidence < 0.7 (e.g. Fig. 10c);
- the presence of some PL identified by rapid mapping procedure on PS imagery but not on S2, (e.g. Figs. 9a, b and 10c) or vice versa (e.g. Figs. 9d and 10c).

Figure 11 reports some selected specific cases. Figure 11c and d clearly show the partial reactivations of badlands, which was positively identified by the PS rapid mapping, confirming the good reliability of the method. Nevetheless while the reactivated areas covered by vegetation in the pre-event phase were well identified, reactivated areas not covered by vegetation in the pre-event phase were not identified. This represents a weakness of the proposed approach.

Figure 11e and f well represent the accuracy of morphological features within the reactivation areas. Another particular case is shown in Fig. 11b, where several landslides mapped by PS rapid mapping were validated by in-situ surveys performed close to urbanized areas and infrastructures (railway line).

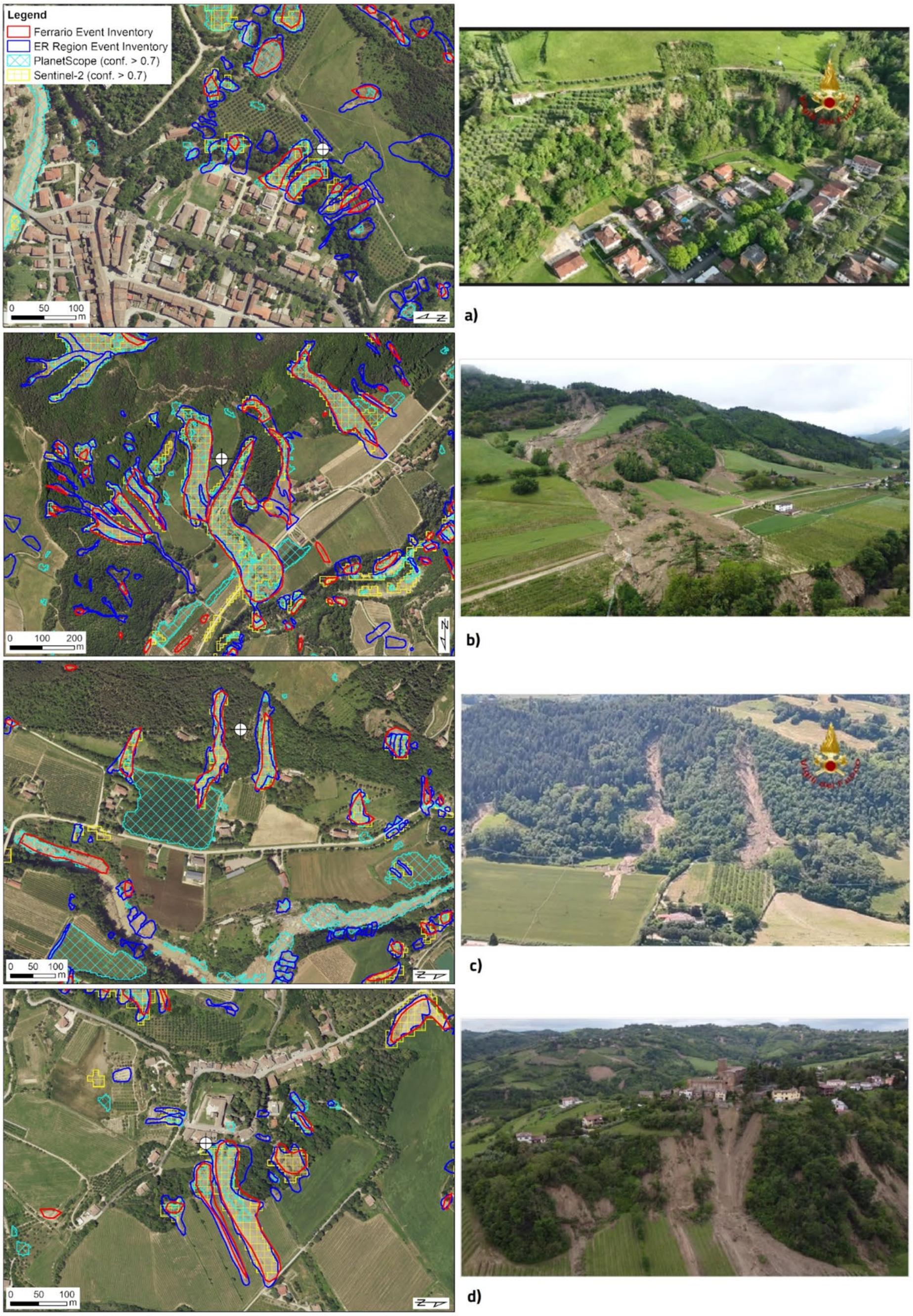

Fig. 9 Comparison of landslide mapped by Ferrario event inventory, ER region event inventory and PL rapid mapping from S2 and PS imagery (confidence > 0.7) (Base map: post-event ortophoto RGBI 20 cm/px). The crosshair in the map allows to match the photo on the right. **a** Dovadola (FC) – Multimedia source: https://www.vigilfuoco.tv; **b** Via Breta, Casola Valsenio (RA)—Photo source: Arpae-SIMC (2023); **c** Casola Valsenio (RA)—Multimedia source: https://www.vigilfuoco.tv; **d** Sorrivoli Castle (FC)—Photo source: Arpae-SIMC (2023d)

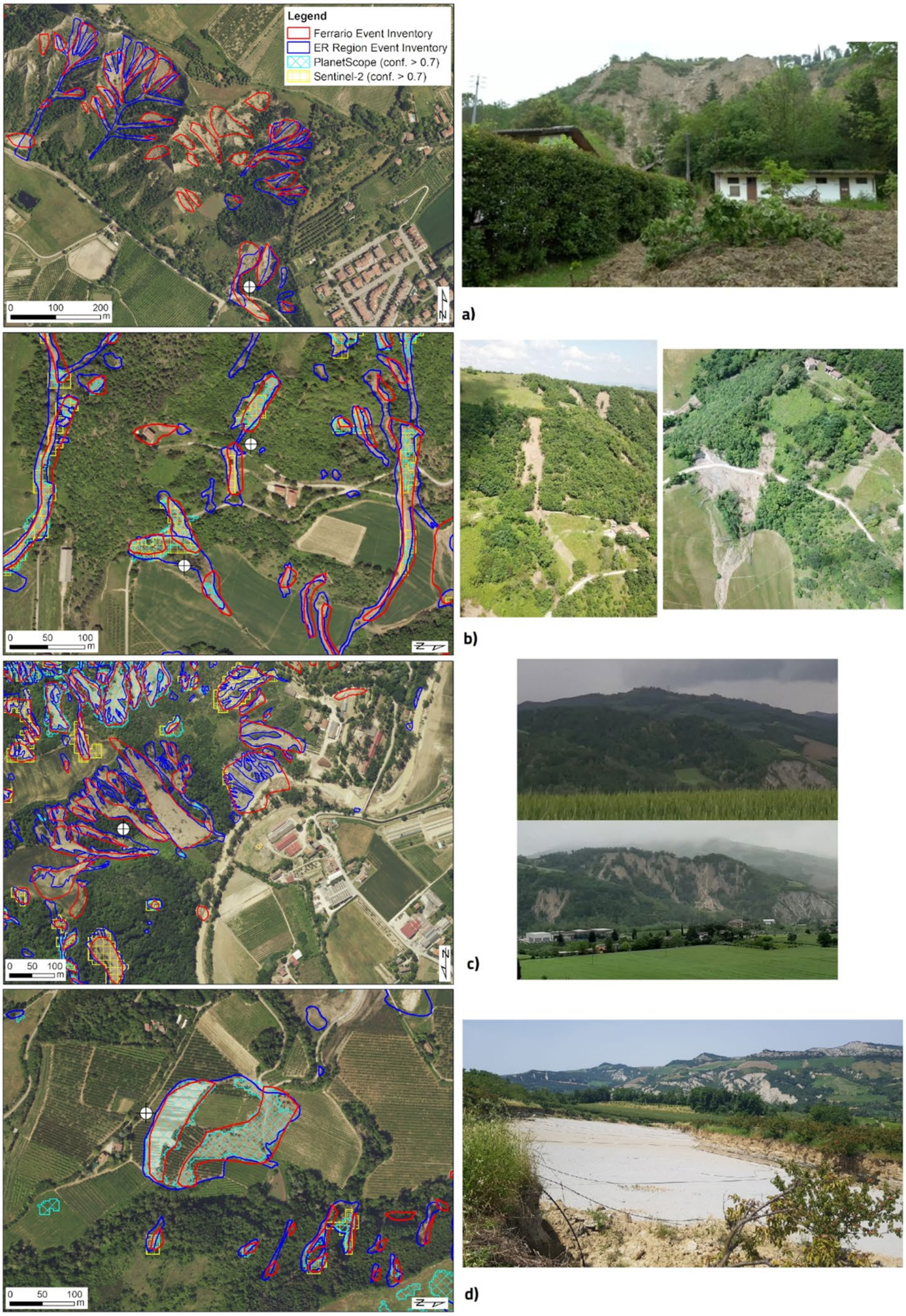

Fig. 10 Comparison of landslide mapped by Ferrario event inventory, ER region event inventory and PL rapid mapping from S2 and PS imagery (confidence > 0.7) (Base map: post-event ortophoto RGBI 20 cm/px). **a** Casalfiumanese (BO)—Multimedia source: https://www.rainews.it/; **b** Via Chiesuola, Casola Valsenio (RA); Photo credits: Giovanni Bertozzi; **c** Pieve salutare (Castrocaro terme, FC)—Multimedia source: Meteo-PedemontanaForlivese; **d** Via Siepi di S. Giovanni—Borgo Tossignano (BO); Photo credits: Saverio Romeo (ISPRA)

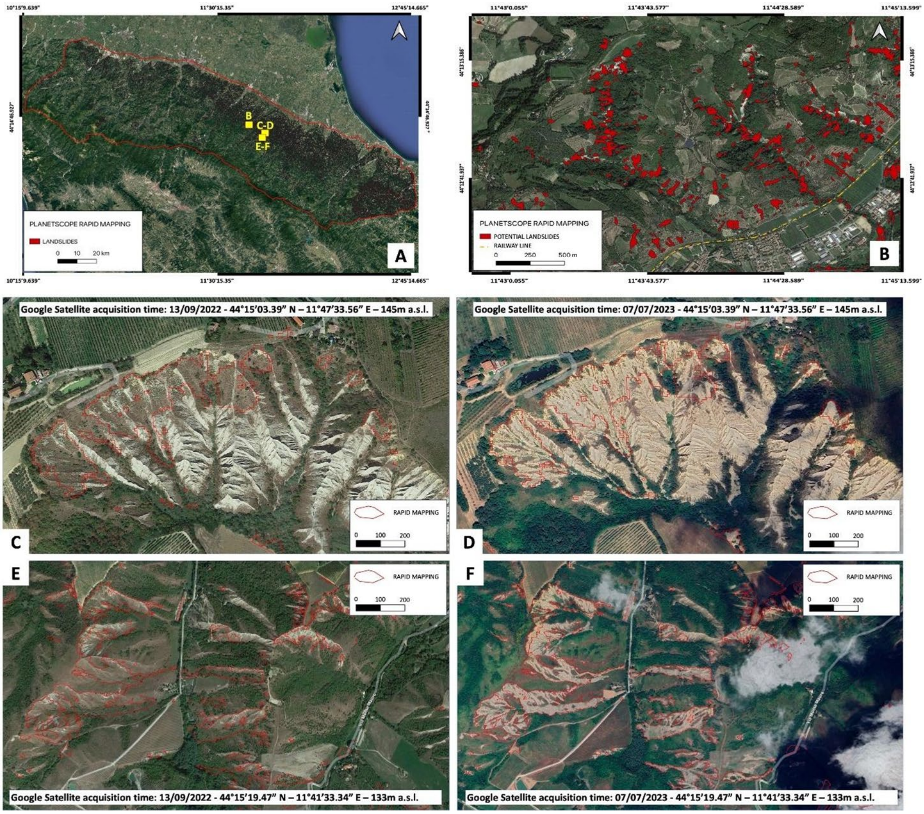

Fig. 11 PL rapid mapping product generated from PS at selected sites (Base map: pre-event and post-event Google Satellite images)

The comparison of the 2023 event landslides with the pre-event landslides recorded in the Italian Landslide Inventory has highlighted that only 1/5 of the landslide area is a reactivation of portions of existing landslides, while 4/5 of the area are newly formed landslides. Bertolini and Pizziolo reported in 2006 that in the previous 50 years, approximately 90% of the large landslides that occurred in the Emilia-Romagna Apennines represented reactivations of dormant landslides.

During March–April 2013 a large number of landslides, mainly small and shallow, occurred in the hilly and mountainous sectors of the Emilia-Romagna region due to heavy rainfall and contemporaneous snow melting (Pizziolo et al. 2015, 2013).

The 2023 event landslides also present peculiar characteristics that distinguish them from the pre-event inventory, especially for their small size (almost 78% of landslides with an area < 1000 m^2) and for the distribution of the slope angle shifted to higher values.

This could be related to the exceptional amount of the two rainfall events that hit in May 2023 the central-eastern territories of Emilia-Romagna, with total precipitation estimated between a quarter and half of the expected value for the entire year (according to 1991–2020 climate data) and estimated return period for each event between 100 and 500 years, depending on the location considered, while the return period is greater than 1,000 years considering the probability that two events of such intensity occurred so close in time (ARPAE 2024).

The increase in recent years of these exceptional/extreme rainfall events triggering mostly shallow and rapid moving landslides is likely connected to climate change in the Mediterranean hotspot (Donnini et al. 2023; Gariano and Guzzetti 2016; Tiranti and Ronchi 2023; Zittis et al. 2022).

7 Conclusions

A fully automated supervised procedure for PL rapid mapping from remote sensing optical multispectral data is presented. Test case used for the procedure development and testing is the heavy rainfall event that hit ER region (Italy) during May, 2023. Although the study was conducted on a single event, findings are general, and landslides rapid mapping products generated from satellite imagery acquired from different satellite sensors consistent. No a-priori threshold is set on the computed confidence measure, leaving to expert operators exploiting the PL rapid mapping product the possibility to generate different scenarios of the distribution of landslide-affected areas.

Generation of PL rapid mapping products and statistics can support effective and efficient response in case of emergency activations. Statistical analysis on administrative units, as well as identification of potential number of affected infrastructures (e.g. roads, railways), can provide useful information to prioritize the interventions to be addressed in emergency response.

Supplementary Information The online version contains supplementary material available at https://doi.org/10.1007/s11069-025-07705-2.

Acknowledgements This work contains modified Copernicus Sentinel data and Copernicus Service information (2023). Sentinel-2 MSI data used were available at no cost from ESA Sentinels Scientific Data Hub. Use of PlanetScope images is under license: ©Planet Labs PBC, CC BY-NC-SA 2.0 (accessed on May 24, 2023). Base map data in Fig. 12 provided by Google. Post-event ortophoto RGBI 20 cm/px available at https://geoportale.regione.emilia-romagna.it/approfondimenti/emergenza-maggio-23/emergenza-rer-maggio-2023-servizi

Author contributions Federico Filipponi: conceptualization, methodology, data collection, analysis, material preparation, writing—original draft, writing—review and editing. Carla Iadanza: conceptualization, investigation, methodology (supporting), data collection, analysis, material preparation, writing—original draft, writing—review and editing. Valerio Vivaldi: data collection, analysis, material preparation, writing—original draft, writing—review and editing. Francesco Zucca: methodology (supporting), data collection, analysis, writing—review and editing. Claudia Meisina: investigation, writing—review and editing. Maria Francesca Ferrario: analysis, writing—review and editing. Alessandro Trigila: conceptualization, investigation, methodology (supporting), writing—review and editing. All authors read and approved the final manuscript.

Funding Open access funding provided by Università degli Studi di Pavia within the CRUI-CARE Agreement. Regarding the contribution of Valerio Vivaldi, this publication is part of the project NODES, funded by the European Union—NextGenerationEU, Mission 4 Component 1.5—ECS00000036—CUP F17G22000190007.

Data availability Outputs from the processing described as rapid mapping landslides inventory in the text are available through ZENODO at https://doi.org/10.5281/zenodo.14199336 with Creative Commons Attribution 4.0 International (Filipponi et al. 2024). The reference data described as Ferrario event inventory in the text is available through ZENODO at https://zenodo.org/records/13234762 with Creative Commons Attribution 4.0 International (Ferrario 2024).

Code availability The analysis was conducted using the developed "Landslides_rapid_mapping" tool, freely available at https://github.com/ffilipponi/LandslidesRapidMapping.

Declarations

Competing interests The authors declare no competing interests.

References

Amatya P, Kirschbaum D, Stanley T, Tanyas H (2021) Landslide mapping using object-based image analysis and open source tools. Eng Geol 282:106000. https://doi.org/10.1016/j.enggeo.2021.106000

Antolini G, Auteri L, Pavan V, Tomei F, Tomozeiu R, Marletto V (2016) A daily high-resolution gridded climatic data set for Emilia-Romagna, Italy, during 1961–2010. Int J Climatol 36:1970–1986. https://doi.org/10.1002/joc.4473

Arpae-SIMC (2023a) L'evento meteo-idrogeologico del 1–4 Maggio 2023. Agenzia Regionale per la Protezione Ambientale Emilia-Romagna (in Italian). https://www.arpae.it/it/notizie/relazione_1-4maggio2023.pdf

Arpae-SIMC (2023b) L'evento meteo-idrogeologico e idraulico del 16–18 Maggio 2023. Agenzia Regionale per la Protezione Ambientale Emilia-Romagna (in Italian). https://www.arpae.it/it/notizie/analisi-evento-16-18-maggio-2023.pdf

Arpae-SIMC (2023c) Rapporto degli eventi meteorologici di piena e di frana dell'1–4 maggio 2023. Agenzia Regionale per la Protezione Ambientale Emilia-Romagna (in Italian). https://www.arpae.it/it/temi-ambientali/meteo/report-meteo/rapporti-post-evento/rapporto_idro_meteo_20230501-04.pdf

Arpae-SIMC (2023d) Rapporto degli eventi meteorologici di piena e di frana del 16–18 maggio 2023. Agenzia Regionale per la Protezione Ambientale Emilia-Romagna (in Italian). https://www.arpae.it/it/temi-ambientali/meteo/report-meteo/rapporti-post-evento/rapporto_idro_meteo_20230516-18.pdf

ARPAE-SIMC (2024) Rapporto IdroMeteoClima Emilia-Romagna Dati 2023. ISBN: 978-88-87854-59-6 (in Italian). https://www.arpae.it/it/temi-ambientali/meteo/report-meteo/rapporti-annuali/rapporto-idrometeoclima-2023

Berti M, Pizziolo M, Scaroni M, Generali M, Critelli V, Mulas M, Tondo M, Lelli F, Fabbiani C, Ronchetti F, Ciccarese G, Dal Seno N, Ioriatti E, Rani R, Zuccarini A, Simonelli T, Corsini A (2025) (2024) RER2023: the landslide inventory dataset of the May 2023 Emilia-Romagna event. Earth Syst Sci Data 17:1055–1074. https://doi.org/10.5194/essd-17-1055-2025

Bertolini G, Pizziolo M (2006) Le grandi frane dell'Emilia-Romagna: stato dell'arte. Il Geologo dell'Emilia-Romagna, anno VI /2006 n.23:33–44 (in Italian).

Brath A, Casagli N, Marani M, Mercogliano P, Motta R (2023) Rapporto della Commissione Tecnico-Scientifica istituita con Deliberazione della Giunta Regionale n. 984/2023 e determinazione dirigenziale 14641/2023, al fine di analizzare gli eventi meteorologici estremi del mese di maggio 2023. Regione Emila-Romagna (in Italian).

Burrows K, Walters RJ, Milledge D, Spaans K, Densmore AL (2020) A new method for large-scale landslide classification from satellite radar. Remote Sens 11:237. https://doi.org/10.3390/rs11030237

Carmignani L, Lazzarotto A, Brogi A, Conti P, Cornamusini G, Costantini A, Meccheri M, Sandrelli F (2004). Carta Geologica della Toscana' Scala 1:250.000.

Castronuovo A (2005) Predisposizione al dissesto per frane superficiali del medio e basso appennino della provincia di Reggio Emilia. Degree Thesis, University of Modena and Reggio Emilia (in Italian)

Cruden DM, Varnes DJ (1996) Landslide Types and Processes, Transportation Research Board, U.S. National Academy of Sciences, Special Report, 247:36–75
Donnini M et al (2023) Landslides triggered by an extraordinary rainfall event in Central Italy on September 15, 2022. Landslides. https://doi.org/10.1007/s10346-023-02109-4
Ferrario MF (2024) Inventory of landslides triggered by heavy rainfall in the Emilia-Romagna region (Italy) in May 2023. Zenodo.https://doi.org/10.5281/zenodo.13234762
Ferrario MF, Livio F (2024) Rapid Mapping of Landslides Induced by Heavy Rainfall in the Emilia-Romagna (Italy) Region in May 2023. Remote Sens 16(1):122. https://doi.org/10.3390/rs16010122
Filipponi F, Smiraglia D, Agrillo E (2022) Earth observation for phenological metrics (EO4PM): temporal discriminant to characterize forest ecosystems. Remote Sens 14(3):721. https://doi.org/10.3390/rs14030721
Filipponi F, Iadanza C, Vivaldi V, Zucca F, Meisina C, Ferrario MF, Trigila A (2024) Rapid mapping inventories of landslides triggered by heavy rainfall in the Emilia-Romagna region (Italy) during May 2023. Zenodo. https://doi.org/10.5281/zenodo.14199336
Filipponi F (in press) Improve Sentinel-2 time series consistency with S2SDB DataBase for operational image co-registration. In: Trends in earth observation, Volume 3 "Earth Observation: current challenges and opportunities for environmental monitoring, pp 162–166
Fiorucci F, Giordan D, Santangelo M, Dutto F, Rossi M, Guzzetti F (2018) Criteria for the optimal selection of remote sensing optical images to map event landslides. Nat Hazards Earth Syst Sci 18(1):405–417. https://doi.org/10.5194/nhess-18-405-2018
Fiorucci F, Ardizzone F, Mondini AC, Viero A, Guzzetti F (2019) Visual interpretation of stereoscopic NDVI satellite images to map rainfall-induced landslides. Landslides 16:165–174. https://doi.org/10.1007/s10346-018-1069-y
Gariano SL, Guzzetti F (2016) Landslides in a changing climate. Earth-Sci Rev 162:227–252. https://doi.org/10.1016/j.earscirev.2016.08.011
Gozza G, Pizziolo M (2007) Analisi del dissesto da frana in Emilia Romagna—Il Progetto IFFI—Metodologia, risultati e rapporti regionali. In: Trigila A. (ed) Rapporto sulle frane in Italia. APAT, Rapporti 78/2007. ISBN: 978-88-448-0310-0 (in Italian)
Guzzetti F, Mondini AC, Cardinali M, Fiorucci F, Santangelo M, Chang KT (2012) Landslide inventory maps: new tools for an old problem. Earth Sci Rev 112(1–2):42–66. https://doi.org/10.1016/j.earscirev.2012.02.001
Hölbling D, Eisank C, Albrecht F, Vecchiotti F, Friedl B, Weinke E, Kociu A (2017) Comparing manual and semi-automated landslide mapping based on optical satellite images from different sensors. Geosciences 7:37. https://doi.org/10.3390/geosciences7020037
Iadanza C, Trigila A, Starace P, Dragoni A, Roccisano M (2021) Biondo t (2021) idroGEO: a collaborative web mapping application based on REST API services and open data on landslides and floods in Italy. ISPRS Int J Geo-Inf 10(2):89. https://doi.org/10.3390/ijgi10020089
Lee S, Min K (2001) Statistical analysis of landslide susceptibility at Yongin, Korea. Environ Geol 40:1095–1113. https://doi.org/10.1007/s002540100310
Lu P, Stumpf A, Kerle N, Casagli N (2011) Object-oriented change detection for landslide rapid mapping. IEEE Geosci Remote Sens Lett 8(4):701–705. https://doi.org/10.1109/LGRS.2010.2101045
Martha TR, Kerle N, Jetten V, van Westen CJ, Kumar KV (2010) Characterising spectral, spatial and morphometric properties of landslides for semi-automatic detection using object-oriented methods. Geomorphology 116(1–2):24–36. https://doi.org/10.1016/j.geomorph.2009.10.004
McFeeters SK (1996) The use of the normalized difference water index (NDWI) in the delineation of open water features. Int J Remote Sens 17(7):1425–1432. https://doi.org/10.1080/01431169608948714
Medley E, Goodman RE (1994) Estimating the block volumetric proportions of melanges and similar block-in matrix rocks (bimrocks). Rock Mechanics, Nelson & Laubach (eds), Balkema, Rotterdam, ISBN 9054103808.
Miller JD, Thode AE (2007) Quantifying burn severity in a heterogeneous landscape with a relative version of the delta normalized burn ratio (dNBR). Remote Sens Environ 109(1):66–80. https://doi.org/10.1016/j.rse.2006.12.006
Mondini AC, Guzzetti F, Reichenbach P, Rossi M, Cardinali M, Ardizzone F (2011) Semi-automatic recognition and mapping of rainfall induced shallow landslides using optical satellite images. Remote Sens Environ 115(7):1743–1757. https://doi.org/10.1016/j.rse.2011.03.006
Montrasio L, Valentino R, Losi GL (2011) Shallow landslides triggered by rainfalls: modeling of some case histories in the Reggiano Apennine (Emilia Romagna Region, Northern Italy). Nat Hazards 60:1231–1254. https://doi.org/10.1007/s11069-011-9906-5
Notti D, Cignetti M, Godone D, Giordan D (2023) Semi-automatic mapping of shallow landslides using free Sentinel-2 images and Google Earth Engine. Nat Hazards Earth Syst Sci 23:2625–2648. https://doi.org/10.5194/nhess-23-2625-2023

Notti D, Cignetti M, Godone D, Cardone D, Giordan D (2024) The unsuPervised shAllow laNdslide rapiD mApping: PANDA method applied to severe rainfalls in northeastern appenine (Italy). Int J Appl Earth Obs Geoinf 129:103806. https://doi.org/10.1016/j.jag.2024.103806

Novellino A, Pennington C, Leeming K, Taylor S, Alvarez IG, McAllister E, Arnhardt C, Winson A (2024) Mapping landslides from space: a review. Landslides. https://doi.org/10.1007/s10346-024-02215-x

Parise M (2001) Landslide mapping techniques and their use in the assessment of the landslide hazard. Phys Chem Earth Part C Ocean Atmos 26(9):697–703. https://doi.org/10.1016/S1464-1917(01)00069-1

Pebesma E (2018) Simple features for R: standardized support for spatial vector data. R J 10(1):439–446. https://doi.org/10.32614/RJ-2018-009

Pebesma E, Bivand R (2023) Spatial Data Science: With applications in R. Chapman and Hall/CRC.

Pieri M, Groppi G (1981) Subsurface geological structure of the Po Plain, Italy. Pubblicazione del Progetto Finalizzato Geodinamica, 414, 23

Pizziolo M, Bernardi M, Daniele G, Generali M, Piacentini D (2015) Landslide occurrences during the high-intensity rainfall event of March–April 2013 in the Emilia-Romagna Region (North Apennines, Italy). In: Lollino G et al (eds) Engineering geology for society and territory, vol 5. Springer International Publishing Switzerland, Cham. https://doi.org/10.1007/978-3-319-09048-1_151

Pizziolo M, Monni A, Primerano S (2013) Con le piogge anomale frane da record. Ecoscienza Numero 2, Anno 2013 (in Italian)

Prakash N, Manconi A, Loew S (2021) A new strategy to map landslides with a generalized convolutional neural network. Sci Rep 11:9722. https://doi.org/10.1038/s41598-021-89015-8

Rouse JJr, Haas RH, Schell JA, Deering DW (1974) Monitoring vegetation systems in the Great Plains with ERTS. NASA Spec. Publ. 1974 351:309.

Satriano V, Ciancia E, Filizzola C, Genzano N, Lacava T, Tramutoli V (2023) Landslides detection and mapping with an advanced multi-temporal satellite optical technique. Remote Sens 15:683. https://doi.org/10.3390/rs15030683

Scheffler D, Hollstein A, Diedrich H, Segl K, Hostert P (2017) AROSICS: an automated and robust open-source image co-registration software for multi-sensor satellite data. Remote Sens 9(7):676. https://doi.org/10.3390/rs9070676

Scheip CM, Wegmann KW (2021) Hazmapper: a global open-source natural hazard mapping application in Google Earth Engine. Nat Hazard 21(5):1495–1511. https://doi.org/10.5194/nhess-21-1495-2021

Schlögl M, Gutjahr K, Fuchs S (2022) The challenge to use multi-temporal InSAR for landslide early warning. Nat Hazards. https://doi.org/10.1007/s11069-022-05289-9

Segoni S, Pappafico G, Luti T, Catani F (2020) Landslide susceptibility assessment in complex geological settings: sensitivity to geological information and insights on its parameterization. Landslides 17:2443–2453. https://doi.org/10.1007/s10346-019-01340-2

Strollo A, Smiraglia D, Bruno R, Assennato F, Congedo L, De Fioravante P, Giuliani C, Marinosci I, Riitano N, Munafò M (2020) Land consumption in Italy. J Maps 16(1):113–123. https://doi.org/10.1080/17445647.2020.1758808

Stumpf A, Kerle N (2011) Object-oriented mapping of landslides using random forests. Remote Sens Environ 115:2564–2577. https://doi.org/10.1016/j.rse.2011.05.013

Tarquini S, Isola I, Favalli M, Battistini A, Dotta G (2023) TINITALY, a digital elevation model of Italy with a 10 meters cell size (Version 1.1). Istituto Nazionale di Geofisica e Vulcanologia (INGV). https://doi.org/10.13127/tinitaly/1.1. Accessed 28 Jul 2024

Tiranti D, Ronchi C (2023) 2023) climate change impacts on shallow landslide events and on the performance of the regional shallow landslide early warning system of Piemonte (northwestern Italy. GeoHazards 4(4):475–496. https://doi.org/10.3390/geohazards4040027

Trigila A, Iadanza C, Spizzichino D (2010) Quality assessment of the Italian Landslide Inventory using GIS processing. Landslides 7:455–470. https://doi.org/10.1007/s10346-010-0213-0

Trigila A, Iadanza C, Esposito C, Scarascia Mugnozza G (2015) Comparison of logistic regression and random forests techniques for shallow landslide susceptibility assessment in Giampilieri (NE Sicily, Italy). Geomorphology 249:119–136. https://doi.org/10.1016/j.geomorph.2015.06.001

Uehara TDT, Sehn Körting T, Soares AR, Quevedo RP (2022) Time-series metrics applied to land use and land cover mapping with focus on landslide detection. J Appl Remote Sens 16(3):034518–034518. https://doi.org/10.1117/1.JRS.16.034518

van Natijne AL, Bogaard TA, van Leijen FJ, Hanssen RF, Lindenbergh RC (2022) World-wide InSAR sensitivity index for landslide deformation tracking. Int J Appl Earth Obs Geoinf 111:102829. https://doi.org/10.1016/j.jag.2022.02829

Vecchiotti F, Tilch N, Kociu A (2021) The use of TERRA-ASTER satellite for landslide detection. Geosciences 11:258. https://doi.org/10.3390/geosciences11060258

Zittis G, Almazroui M, Alpert P, Ciais P, Cramer W, Dahdal Y et al (2022) Climate change and weather extremes in the Eastern Mediterranean and Middle East. Rev Geophys 60:e2021RG000762. https://doi.org/10.1029/2021RG000762

Publisher's note Springer Nature remains neutral with regard to jurisdictional claims in published maps and institutional affiliations.

Authors and Affiliations

Federico Filipponi[1] · Carla Iadanza[2] · Valerio Vivaldi[3] · Francesco Zucca[3] · Claudia Meisina[3] · Maria Francesca Ferrario[4] · Alessandro Trigila[2]

✉ Valerio Vivaldi
valerio.vivaldi@unipv.it

1 Italian National Research Council (CNR), Institute of Environmental Geology and Geoengineering (IGAG), Rome, Italy

2 Italian Institute for Environmental Protection and Research (ISPRA), Rome, Italy

3 Department of Earth and Environmental Sciences, University of Pavia, Pavia, Italy

4 Department of Science and High Technology, Università degli Studi dell'Insubria, Como, Italy